

#### **ARTICLE**

# ESCRT-I and PTPN23 mediate microautophagy of ubiquitylated tau aggregates

Yusen Men<sup>1\*</sup>, Shoshiro Hirayama<sup>1\*</sup>, Shinpei Ao<sup>1</sup>, Yasuyuki Sakurai<sup>1</sup>, Yuri Shibata<sup>1</sup>, Megan Lo<sup>1</sup>, Yusuke Sato<sup>2</sup>, and Shigeo Murata<sup>1</sup>

Protein aggregates are degraded by both the autophagy-lysosomal and the ubiquitin-proteasome pathways. Macroautophagy and microautophagy, two forms of the autophagy-lysosomal pathway, are widely conserved across eukaryotes. While macroautophagy has been extensively studied in the context of degradation of protein aggregates, microautophagy remains less explored. Here, we identify the UBAP1-containing ESCRT-I complex and PTPN23 as new regulators for degradation of aggregated proteins through an unbiased genome-wide CRISPR knockout screen, using a cell line expressing tau repeat domain (tauRD) aggregates. ESCRT-I recognizes ubiquitylated tauRD via the UEV domain of TSG101. The accessory protein PTPN23, instead of ESCRT-II, bridges ESCRT-I and ESCRT-III to complete the endosomal microautophagy of ubiquitylated tauRD aggregates. Our results uncover the molecular mechanism underlying the degradation of tau aggregates by endosomal microautophagy.

### Introduction

The formation of misfolded protein aggregates is a hallmark of neurodegenerative diseases (Sweeney et al., 2017). Such aberrant, aggregation-prone misfolded proteins in the cytoplasm have been reported to be cleared via both the autophagy-lysosomal pathway and the ubiquitin-proteasome system (UPS) (Ciechanover and Kwon, 2015; Mee Hayes et al., 2022). Generally, it is believed that protein aggregates are cleared via the autophagy-lysosomal pathway, whereas proteasomes can only degrade small soluble oligomers (Ciechanover and Kwon, 2015; Mee Hayes et al., 2022).

Autophagy in mammals is categorized into three types: macroautophagy, microautophagy, and chaperone-mediated autophagy (CMA) (Bejarano and Cuervo, 2010). Macroautophagy has a well-established role in delivering cytoplasmic protein aggregates to lysosomes via double-membraned autophagosomes. In contrast, CMA selectively targets soluble proteins with KFERQ-like motifs for direct transport into lysosomes and is believed to be incapable of degrading protein aggregates (Bejarano and Cuervo, 2010; Kaushik and Cuervo, 2018; Martinez-Vicente et al., 2008). However, whether and how microautophagy mediates the degradation of cytosolic protein aggregates remains unclear.

Microautophagy is classified into two types: lysosomal membrane protrusion or invagination (lysosomal microautophagy) and endosomal membrane invagination (endosomal microautophagy) (Kuchitsu and Taguchi, 2023; Oku and Sakai, 2018). Mechanistically, endosomal microautophagy partially resembles the canonical endocytic pathway. In the canonical endocytic pathway, the endosomal sorting complexes required for transport (ESCRT) machinery, which consists of four distinct

complexes, ESCRT-0, ESCRT-I, ESCRT-II, and ESCRT-III, sequentially sorts proteins into endosomes and directs them toward lysosomal degradation (Vietri et al., 2020; Williams and Urbé, 2007). However, certain types of endosomal microautophagy have been reported to depend on different factors (Kuchitsu and Taguchi, 2023; Sakai and Oku, 2024), and a comprehensive understanding of the molecular factors that execute each type of microautophagy remains elusive.

In this study, we revealed that the UBAP1-containing ESCRT-I complex and the UBAP1-binding protein PTPN23 function in endosomal microautophagy of ubiquitylated protein aggregates, which we term microaggrephagy, using a cell model that stably propagates amyloidogenic tau repeat domain (tauRD) through a genome-wide CRISPR knockout (KO) screen. We further showed that ectopic expression of the UBAP1 disease variant identified in hereditary spastic paraplegia (HSP) patients, which lacks the PTPN23 binding region, leads to a significant accumulation of tauRD aggregates (Nan et al., 2019; Wang et al., 2020; Lin et al., 2019; Farazi Fard et al., 2019; Gu et al., 2020; Bourinaris et al., 2020). Our research provides insight into the substrate recognition and transfer mechanisms of microaggrephagy.

#### Results

Identification of the ESCRT machinery as a regulator of tauRD (P301L) accumulation via a genome-wide CRISPR KO screen
To identify factors that regulate the accumulation of amyloid-like tau, we established a HEK293A cell line stably expressing

<sup>1</sup>Laboratory of Protein Metabolism, Graduate School of Pharmaceutical Sciences, The University of Tokyo, Tokyo, Japan; <sup>2</sup>Department of Chemistry and Biotechnology and Center for Research on Green Sustainable Chemistry, Graduate School of Engineering, Tottori University, Tottori, Japan.

\*Y. Men and S. Hirayama contributed equally to this paper. Correspondence to Shigeo Murata: smurata@g.ecc.u-tokyo.ac.jp.

© 2025 Men et al. This article is distributed under the terms as described at https://rupress.org/pages/terms102024/.





tauRD (residues 244–372 in the 2N4R isoform of full-length tau), the minimal region required for amyloid fibril formation (Eliezer et al., 2005). We introduced a P301L mutation, originally identified in patients with frontotemporal dementia, to enhance the aggregation propensity of tauRD (Von Bergen et al., 2001; Barghorn et al., 2000) and tagged it with the fluorescent protein Venus for visualization and quantification (Nagai et al., 2002) (Fig. S1 A). We transfected preformed tauRD (P301L) amyloid fibrils into cells as described in a previous study (Sanders et al., 2014). We established a cell line stably propagating tauRD (P301L) aggregates, which was confirmed by fluorescence microscopy (Fig. S1 B).

We found that tauRD (P301L) aggregates colocalized with ubiquitin (Fig. S1 C). Biochemical analysis showed that Triton X-100-insoluble tauRD (P301L) was heavily phosphorylated compared with Triton X-100-soluble tauRD (P301L) (Fig. S1 D), similar to physiological tau found in the neuronal cells of Alzheimer's disease brains (Cripps et al., 2006; Ferrer et al., 2013; Grundke-Iqbal et al., 1986). To determine the relative contribution of proteasomal degradation and lysosomal degradation to the clearance of tauRD (P301L), we treated cells with inhibitors of each pathway. Treatment with the proteasome inhibitor bortezomib (BTZ), the lysosome proton pump inhibitor bafilomycin A1 (BafA1), or their combination led to significant accumulation of tauRD (P301L) (Fig. S1 E), consistent with reports that tau is degraded by both proteasomes and lysosomes (Lee et al., 2013). These results suggest that tauRD (P301L) has properties consistent with amyloidogenic tau, validating the suitability of the established cell line for screening regulators of tau aggregates.

Using this cell line, we performed a genome-wide CRISPR KO screen to identify factors regulating tau accumulation (Fig. 1 A). We identified 486 genes, excluding those with a P value of 0.05 or higher, from the top 500 β-score genes, whose KO increased fluorescence intensity of tauRD (P301L) (Fig. 1 B). Among the top hits were proteasome subunits and the AAA ATPase valosin-containing protein (VCP)/p97 (Fig. 1 B), which assists proteasomal degradation, validating the screening approach. Furthermore, protein-protein association network analysis of the candidate genes revealed four distinct gene clusters: RNA splicing factors, the ESCRT machinery, the UPS, and chaperonins (Fig. 1 C), the latter two of which have been extensively studied in the context of amyloidogenic protein degradation (Shimura et al., 2004; Kitamura et al., 2006). The KO of RNA splicing factors causes a wide range of effects, and thus, their identification was likely nonspecific. Additionally, since we used the tauRD (P301L) cDNA that lacked introns, any effect of KO of RNA splicing factors on tauRD (P301L) is likely indirect. We therefore focused on the ESCRT machinery.

The ESCRT machinery consists of four distinct complexes, ESCRT-0, ESCRT-I, ESCRT-II, and ESCRT-III, that mediate endolysosomal sorting of ubiquitylated cargos, multivesicular body biogenesis, and microautophagy (Williams and Urbé, 2007; Majumder and Chakrabarti, 2016). We identified four subunits of ESCRT-I, four subunits of ESCRT-III, and two accessory factors of the ESCRT machinery among the top 500 hits from our CRISPR KO screen (Fig. S1 F) but did not detect any subunits of

ESCRT-0 and ESCRT-II. The ESCRT-I subunits MVB12 and VPS37 have several homologs in mammalian cells. Our screen identified the ESCRT-I complex containing UBAP1 (a member of the MVB12 family) and VPS37A (a member of the VPS37 family) as a regulatory factor for tauRD aggregates (Fig. S1 F). This is consistent with a previous study showing that VPS37A, but not VPS37B or VPS37C, specifically interacts with UBAP1 and that UBAP1 is selectively incorporated into the VPS37A-containing ESCRT-I complex (Wunderley et al., 2014; Stefani et al., 2011).

We did not observe any candidates functioning in the macroautophagy or CMA pathways in our CRISPR KO screen. Indeed, KO of the core macroautophagy factors ATG7 and FIP200 and the CMA protein LAMP2 did not result in significant accumulation of tauRD (P301L) compared with that of any of the UPS-related proteins, including proteasome subunits PSMA6 (a1) and PSMD7 (Rpn8) and VCP, or the ESCRT proteins TSG101 and PTPN23 (Fig. S1, G and H). This result suggests that neither macroautophagy nor CMA is significantly involved in tauRD (P301L) clearance in HEK293A cells and that the effect of BafA1 observed in our model is likely primarily due to the inhibition of microautophagy (Fig. S1 E). To further confirm that the effect of ESCRT machinery depletion is not due to altered proteasome degradation, we measured the proteasome peptidase activity under ESCRT protein knockdown. None of the knockdowns altered proteasome activity, in contrast to BTZ treatment, which almost completely abolished it (Fig. S1 I). Together with the results showing that depletion of ESCRT proteins did not change the levels of UPS-related proteins (Fig. S1 H), these data raise the possibility that the ESCRT machinery specifically regulates the accumulation of tauRD (P301L) through microautophagy.

To confirm the effect of ESCRT machinery KO on tauRD (P301L) accumulation, we knocked out individual components of each ESCRT complex and the accessory factor PTPN23 using sgRNA in the cell line used for the screen (Fig. 1 D). VCP, a hypomorphic mutation of which has recently been demonstrated to cause tau accumulation in the brain tissues of AD patients and knock-in mice (Darwich et al., 2020), was used as a positive control. In the ESCRT-0 complex, KO of HRS but not STAM caused accumulation of tauRD (P301L) (Fig. 1 D). Depletion of the ESCRT-I subunits TSG101, UBAP1, VPS28, and VPS37, as well as the ESCRT accessory factor His domain phosphotyrosine phosphatase (HD-PTP)/PTPN23, resulted in significantly greater accumulation of tauRD (P301L) (Fig. 1 D) compared with HRS KO. KO of ESCRT-II did not have a significant effect on tauRD (P301L) accumulation, consistent with the results of our screen (Fig. 1 D and Fig. S1 F). In the ESCRT-III complex, only depletion of CHMP1A significantly affected tauRD (P301L) accumulation. While depletion of other ESCRT-III subunits also increased tauRD (P301L) levels, these changes did not reach statistical significance (Fig. 1 D). Considering the functional redundancy of ESCRT-III subunits, we further tested the combined knockdown of CHMP4A, CHMP4B, and CHMP4C and the double knockdown of VPS4A and VPS4B, the AAA ATPases involved in the disassembly of the ESCRT-III complex (Arii et al., 2018; Szymańska et al., 2020). Simultaneous depletion of CHMP4A, CHMP4B, and CHMP4C (CHMP4A/B/C) resulted in significant accumulation of tauRD (P301L) (Fig. 1 E), with CHMP4B knockdown having the



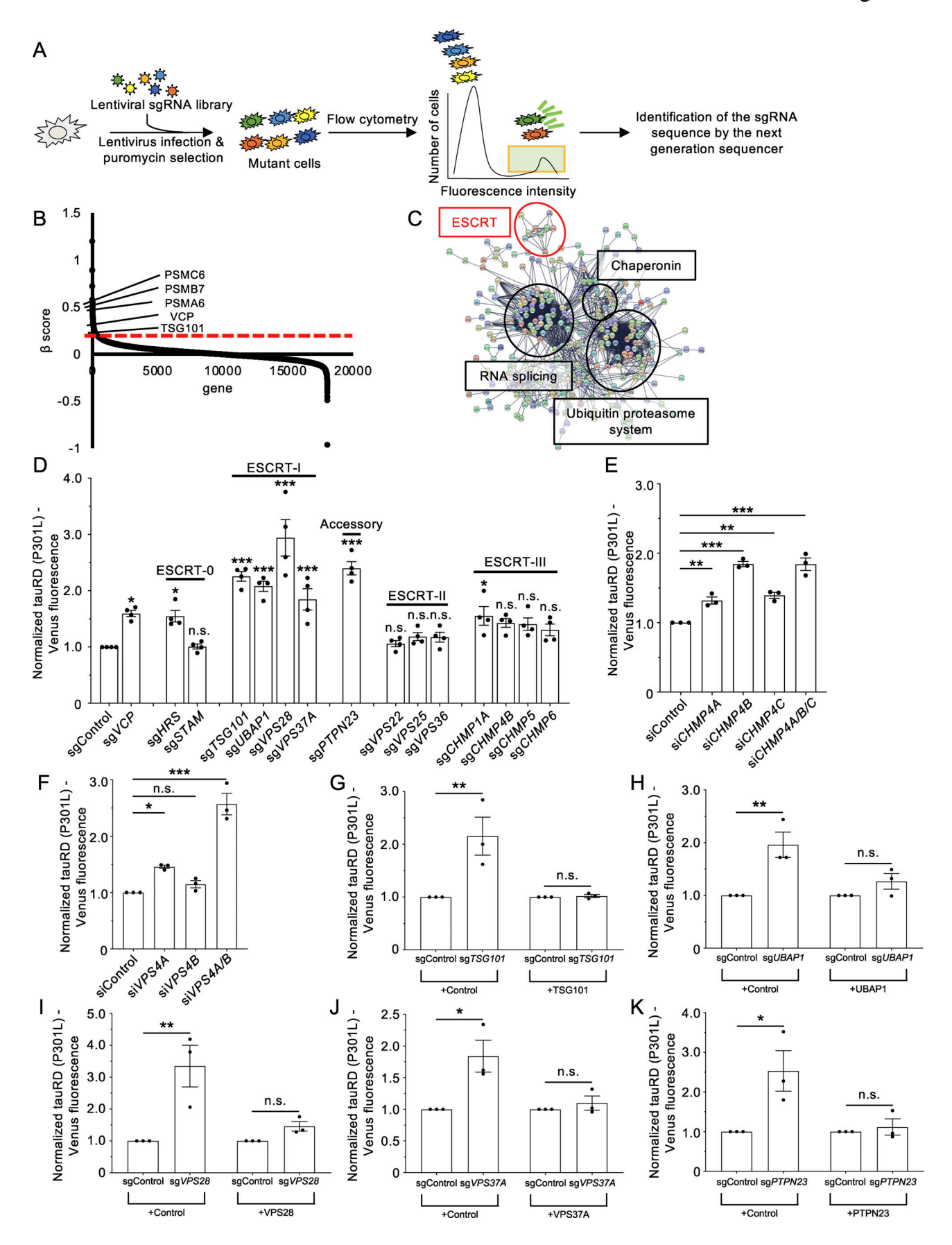


Figure 1. Genome-wide CRISPR KO screen identified ESCRT machinery as a regulator of tauRD (P301L) clearance. (A) Schematic diagram of the genome-wide CRISPR KO screen. (B)  $\beta$ -score plot of all genes used in the CRISPR KO screen with the cutoff value of positive hits denoted as a red dashed line.



486 candidate genes were identified in the screen. Selected proteasome subunits, the proteasome accessory factor VCP, and the ESCRT-I complex subunit TSG101 are labeled. **(C)** Known and predicted protein–protein interactions among the 486 candidates identified in the CRISPR KO screen based on STRING analysis (ver11.5). **(D)** TauRD (P301L)-Venus aggregate–positive cells were transfected with control or individual sgRNA, as indicated, and successfully transfected cells were selected by puromycin treatment. TauRD (P301L)-Venus fluorescence was measured by flow cytometry 1 wk after transfection. Data were normalized to the Venus fluorescence of sgControl-treated cells and represent the mean  $\pm$  SEM (n = 4, from four independent experiments). Significance was calculated using one-way ANOVA with Dunnett's test with \*P < 0.05, \*\*\*P < 0.001. n.s., not significant. **(E)** TauRD (P301L)-Venus aggregate–positive cells were transfected with control, *CHMP4A*, *CHMP4B*, *CHMP4C*, or *CHMP4A/B/C* siRNA. TauRD (P301L)-Venus fluorescence was measured by flow cytometry 72 h after transfection. Data were normalized to the Venus fluorescence of siControl-treated cells and represent the mean  $\pm$  SEM (n = 3, from three independent experiments). Significance was calculated using one-way ANOVA with Dunnett's test with \*P < 0.01, \*\*\*P < 0.001. **(F)** TauRD (P301L)-Venus aggregate–positive cells were transfected with control, *VPS4A*, *VPS4B*, or *VPS4A/B/s*iRNA and analyzed as in E. Data were normalized to the Venus fluorescence of siControl-treated cells and represent the mean  $\pm$  SEM (n = 3, from three independent experiments). Significance was calculated using one-way ANOVA with Dunnett's test with \*P < 0.05, \*\*\*P < 0.001. n.s., not significant. **(G-K)** TauRD (P301L)-Venus aggregate–positive cells stably expressing mCherry (Control) or mCherry-tagged sgRNA-resistant variants of TSG101 (G), UBAP1 (H), VPS28 (I), VPS37A (J), and PTPN23 (K) were transfected with individual sgRNA of ESCRT-I complex subunits and analyzed as in D. D

strongest individual effect. In contrast, knockdown of VPS4A or VPS4B alone had minimal to no effect on tauRD (P301L) accumulation (Fig. 1 F), whereas their combined depletion resulted in a more pronounced accumulation (Fig. 1 F). KO and knockdown of each subunit were validated by western blot or qPCR (Fig. S2, A-G). These results suggest that UBAP1-containing ESCRT-I, PTPN23, and ESCRT-III contribute to the clearance of tauRD (P301L).

To exclude the possibility of off-target effects from our sgRNA KO of ESCRT-I and PTPN23, we performed rescue experiments by stably expressing sgRNA-resistant variants of TSG101, UBAP1, VPS28, VPS37A, and PTPN23 in tauRD (P301L) aggregate-positive cells, followed by KO of each endogenous component. Depletion of each subunit increased the tauRD (P301L) fluorescence signal in control cells, but no effect was observed in cells stably expressing exogenous sgRNA-resistant ESCRT-I and accessory subunits (Fig. 1, G-K and Fig. S2, H-L). These results indicate that tauRD (P301L) accumulation is specifically associated with dysfunction of UBAP1-containing ESCRT-I and PTPN23.

### ESCRT-I mediates the degradation of amyloidogenic tauRD (P301L) via endosomal microautophagy

To determine whether the ESCRT machinery is involved in degrading aggregated tauRD (P301L), we performed pulse-chase experiments using cells stably expressing tauRD (P301L)-Flag-Halo aggregates. Cells were incubated with the TMR ligand to label the preexisting population of tauRD (P301L)-Flag-Halo before washout. TMR fluorescence intensity was measured at three time points after washout. Knockdown of TSG101, an essential subunit in endosomal sorting, significantly slowed the turnover rate of tauRD (P301L) compared with control cells (Fig. 2 A and Fig. S3 A). In contrast, TSG101 knockdown did not affect the turnover rate of Flag-Halo (Fig. 2 B and Fig. S3 A), suggesting that TSG101 specifically targets amyloidogenic tauRD (P301L).

Previous studies have shown that tau can be secreted unconventionally across the plasma membrane (Katsinelos et al., 2018; Merezhko et al., 2018). A recent study also reported that loss-of-function in the ESCRT pathway can promote the escape of tau seeds from compromised endolysosomal membranes and the subsequent propagation of tau aggregates (Chen et al., 2019).

To exclude the possibility that the observed effects of TSG101 knockdown were due to increased secretion and propagation of tauRD (P301L), we first assessed the amount of secreted tauRD (P301L). Immunoprecipitation of the cell culture medium revealed extremely limited levels of tauRD (P301L) following TSG101 knockdown (Fig. S3 B). We further cocultured tauRD (P301L)-Venus aggregate-positive cells with tauRD (P301L)mCherry aggregate-negative cells. Flow cytometry detected a small population (~1.5%) of tauRD (P301L)-Venus in aggregatenegative cells after coculture, and this population increased only slightly and not significantly under TSG101 knockdown, and immunoblotting barely detected their presence (Fig. S3, C-E). These results suggest that while a minor fraction of tauRD (P301L) may undergo secretion and spread to other cells, the levels are negligible. Thus, the primary effects of ESCRT depletion are impaired degradation of aggregated tauRD (P301L) within cells.

Two forms of microautophagy function in protein degradation: lysosomal microautophagy and endosomal microautophagy (Kuchitsu and Taguchi, 2023; Oku and Sakai, 2018). The ESCRT machinery has been implicated in both types of microautophagy (Kuchitsu and Taguchi, 2023; Oku and Sakai, 2018). To determine which microautophagy pathway is mediated by the ESCRT machinery in degrading aggregated tauRD, we examined the localization of tauRD (P301L) aggregates within the endolysosomal pathway under the addition of lysosomal protease inhibitors E64 and pepstatin A. First, we immunostained for EEA1, an early endosome marker, in tauRD (P301L) aggregate-positive cells. Three-dimensional imaging using super-resolution microscopy revealed that small tauRD (P301L) aggregates were encapsulated within EEA1-positive endosomes (Fig. 2 C). Next, we expressed constitutively active Rab7A (Q67L), a late endosome marker, in tauRD (P301L) aggregate-positive cells and found that small tauRD (P301L) aggregates were also contained within Rab7A (Q67L)-positive endosomes (Fig. 2 D). In addition, we immunostained for LAMP1, a lysosome marker, in tauRD (P301L) aggregate-positive cells. Although we were unable to image the LAMP1-labeled structures in three dimensions due to the size limitations, we observed colocalization between LAMP1positive lysosomes and tauRD (P301L) aggregates (Fig. 2 E). These results suggest that degradation of tauRD (P301L) aggregates occurs through the endosomal microautophagy pathway.



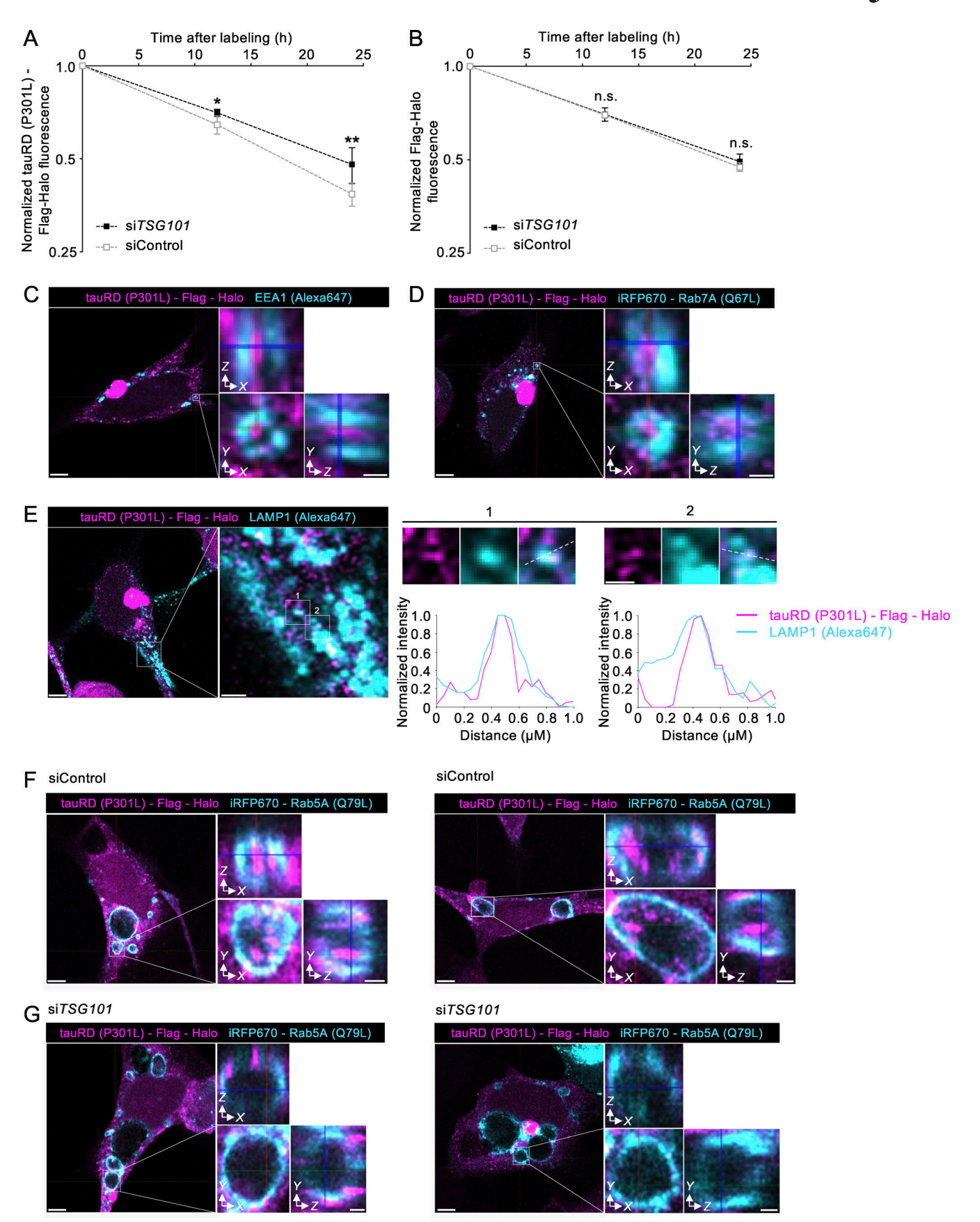


Figure 2. **ESCRT-I mediates degradation of tauRD (P301L) aggregates via endosomal microautophagy. (A and B)** TSG101 specifically targets tauRD (P301L) over Flag-Halo. TauRD (P301L)-Flag-Halo aggregate—positive cells (A) or HEK293A cells stably expressing Flag-Halo (B) were transfected with control



or TSG101 siRNA. 50 nM TMR ligand was added for 30 min 72 h after transfection, followed by two washes with PBS. Fluorescence of tauRD (P301L)-Flag-Halo (A) or Flag-Halo (B) was measured at 0, 12, and 24 h after TMR washout by flow cytometry. Data were normalized to the TMR fluorescence of cells at 0 h after TMR labeling and represent the mean  $\pm$  SD (A, n=4, from four independent experiments; B, n=3, from three independent experiments). Significance was calculated using two-way ANOVA with Bonferroni's test with \*P < 0.05, \*\*P < 0.01. n.s., not significant. (**C and D**) Three-dimensional visualization of tauRD (P301L)-Flag-Halo aggregates in early and late endosomes. Cells were immunostained with an antibody against the early endosome marker EEA1 antibody (C) or transfected with iRFP670-Rab7A (Q67L) for visualization of the late endosome (D). The cells were fixed and imaged by super-resolution microscopy 48 h after transfection. Scale bar: 5  $\mu$ m and 500 nm (magnified images). (**E**) Colocalization between LAMP1 and tauRD (P301L)-Flag-Halo aggregates. Cells were immunostained with the lysosome marker LAMP1 antibody and imaged by super-resolution microscopy. Boxed areas are magnified, and line profiling of a representative section of the cell indicated by a white dashed line is shown on the right. Scale bar: 5  $\mu$ m, 1  $\mu$ m (magnified images), and 500 nm (magnified view of boxed areas 1 and 2). For the inhibition of lysosomal proteolysis, E64d (10  $\mu$ g/ml) and pepstatin A (10  $\mu$ g/ml) were added to the medium 8 h before imaging in C-E. (**F and G**) TSG101 was required for encapsulation of tauRD (P301L)-Flag-Halo aggregates in early endosomes. TauRD (P301L)-Flag-Halo aggregate-positive cells were transfected with control (F) or TSG101 siRNA (G) and iRFP670-Rab5A (Q79L). 50 nM TMR ligand was added 24 h after transfection. The cells were fixed and imaged by super-resolution microscopy 48 h after transfection. Scale bar: 5 and 1  $\mu$ m (magnified images).

To further confirm the critical role of the ESCRT machinery in this process, we expressed Rab5A (Q79L) in tauRD (P301L) aggregate-positive cells. This mutant Rab5A remains in the GTPbound state, enhancing endosome fusion and causing enlargement of early and late endosomes. These enlarged endosomes can be readily used to visualize the uptake of substrates of endosomal microautophagy (Ceresa et al., 2001). We observed that small tauRD (P301L) aggregates were encapsulated within Rab5A (Q79L)-positive endosomes (Fig. 2 F). Furthermore, TSG101 knockdown disrupted the localization of tauRD (P301L) aggregates to the endosomal lumen (Fig. 2 G). In addition to TSG101, the ESCRT-III subunits CHMP4 and VPS4, identified as regulators of tauRD (P301L) (Fig. 1, D and E), have been reported as essential for endosomal microautophagy (Tekirdag and Cuervo, 2018; Sahu et al., 2011; Mukherjee et al., 2016). Taken together, these findings suggest that the ESCRT machinery mediates endosomal microautophagy of tauRD (P301L) aggregates.

## Inhibition of ESCRT-mediated endosomal microautophagy leads to enlargement of tauRD (P301L) aggregates and accumulation of K48- and K63-ubiquitylated tauRD (P301L)

In addition to the accumulation of tauRD (P301L), we observed that TSG101 depletion led to an enlargement of tauRD (P301L) aggregates (Fig. 2, F and G). Accordingly, we quantitatively analyzed changes in aggregate size following the inhibition of proteasomes, lysosomes, and the ESCRT pathway (Fig. 3, A-D). Lysosome inhibition significantly increased the size of tauRD (P301L) aggregates compared with proteasome inhibition (Fig. 3 B). As we demonstrated that neither macroautophagy nor CMA pathways are major pathways of tauRD (P301L) clearance (Fig. S1 H), this result suggests that the enlargement of tauRD (P301L) aggregates is primarily due to microautophagy inhibition. Next, we quantified the size of tauRD (P301L) aggregates under conditions of TSG101, CHMP4A/B/C, and VPS4A/B knockdown, as well as PTPN23 KO. Depletion of any of these subunits caused significant enlargement of tauRD (P301L) aggregates, similar to the effects of lysosome inhibition (Fig. 3, C and D). These findings suggest that inhibiting ESCRT-mediated endosomal microautophagy causes significant accumulation of aggregated tauRD (P301L).

We biochemically analyzed the effects of impaired ESCRT-mediated endosomal microautophagy. Western blot analysis showed that TSG101 knockdown markedly increased Triton X-

100-insoluble tauRD (P301L) (Fig. 3 E, lanes 7 and 8). We immunoprecipitated tauRD (P301L) from both Triton X-100-soluble and Triton X-100-insoluble fractions following solubilization of the insoluble fraction with 0.5% sodium dodecyl sulfate (SDS). Triton X-100-insoluble tauRD (P301L) was heavily modified with ubiquitin chains under TSG101 knockdown conditions (Fig. 3 E, lanes 7 and 8). To identify the type of ubiquitin chains on insoluble tauRD (P301L), we performed ubiquitin chain restriction (UbiCRest) analysis, a technique that utilizes ubiquitin chain type-specific deubiquitinases to cleave ubiquitin chains on the substrate to determine the type of ubiquitin chain linkage (Hospenthal et al., 2015). We treated immunoprecipitated Triton X-100-insoluble tauRD (P301L) with the K48-specific deubiquitinase OTUB1, the K63-specific deubiquitinase AMSH-LP, or both (Fig. S4, A and B). Treatment with either OTUB1 or AMSH-LP reduced the ubiquitin chain levels on tauRD (P301L), and their combination nearly abolished the ubiquitylation (Fig. 3 F). These results indicate that tauRD (P301L) is ubiquitylated with both K48- and K63-linked chains, which are thought to be recognized by the ESCRT machinery (Strickland et al., 2022; Waltho et al., 2024).

### The ubiquitin E2 variant domain of TSG101 is necessary for recognition of ubiquitylated tauRD (P301L)

To evaluate the importance of tauRD (P301L) ubiquitylation for its clearance, we treated tauRD (P301L) aggregate-positive cells with TAK-243, an inhibitor of the ubiquitin-activating enzyme, which caused significant accumulation of tauRD (P301L) (Fig. 4 A). Treatment with TAK-243 also enlarged tauRD (P301L) aggregates (Fig. 4 B). These results confirm that ubiquitylation is necessary for tauRD (P301L) degradation.

Among ESCRT-I, PTPN23, and ESCRT-III, only the ESCRT-I subunits TSG101 and UBAP1 contain ubiquitin-binding domains (Fig. 4 C). TSG101 contains a ubiquitin E2 variant (UEV) domain at its N terminus that interacts with ubiquitin, whereas UBAP1 contains a solenoid of overlapping UBA (SOUBA) domain at its C terminus that binds to K48- and K63-linked polyubiquitin chains (Sundquist et al., 2004; Agromayor et al., 2012). To identify which ubiquitin-binding domain is required for the recognition and degradation of ubiquitylated tauRD (P301L) aggregates, we generated TSG101 and UBAP1 mutants lacking their respective ubiquitin-binding domains. *UBAP1* KO and *TSG101* knockdown markedly increased tauRD (P301L) accumulation in control mCherry-expressing cells (Fig. 4, D and E, black columns; and



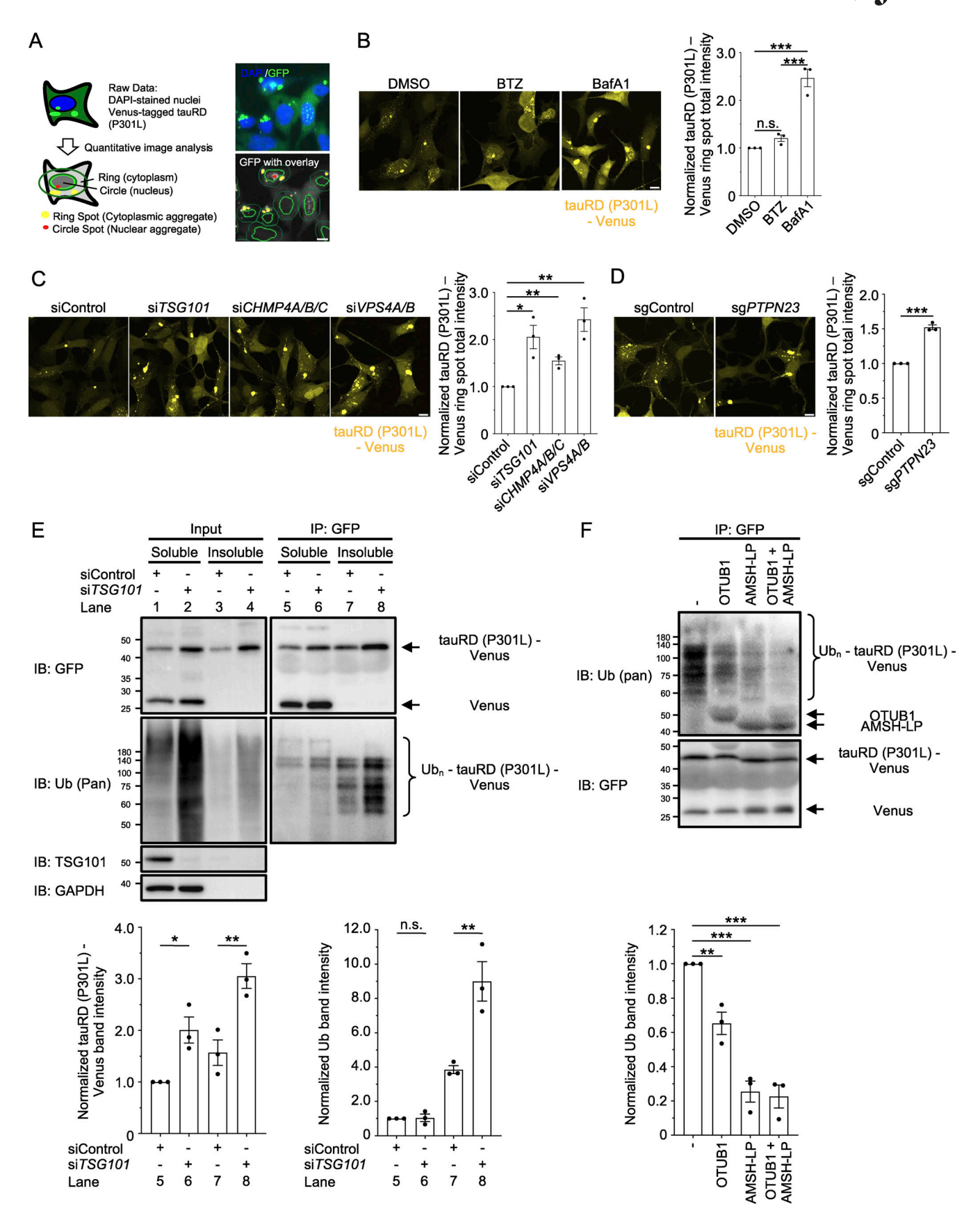


Figure 3. ESCRT depletion resulted in enlargement of tauRD (P301L) aggregates and an increased population of ubiquitylated insoluble tauRD (P301L). (A) Schematic of tauRD (P301L)-Venus aggregate detection and quantification by a high-content image analyzer. Raw data consisting of DAPI-stained nuclei and GFP (Venus) fluorescence were obtained. The area of DAPI fluorescence was used to define the nucleus (circle), and a region of set width around the

Men et al. Journal of Cell Biology https://doi.org/10.1083/jcb.202406120



nucleus (ring) was used as the cytoplasm. Bright spots made by Venus within the circle and ring were defined as nuclear (red) and cytoplasmic (yellow) tauRD (P301L)-Venus aggregates, respectively. Ring spot total intensity was used to measure the size of cytoplasmic tauRD (P301L)-Venus aggregates. Scale bar: 10 μm. (B-D) Ring spot total intensity of tauRD (P301L)-Venus aggregates was quantified by a high-content image analyzer, and cells were imaged by a confocal microscope. TauRD (P301L)-Venus aggregate-positive cells were treated with 500 nM BTZ or 1 μM BafA1 (B), transfected with control, TSG101, CHMP4A/B/C, or VPS4A/B siRNA (C), or transfected with control or PTPN23 sgRNA, and successfully transfected cells were selected by puromycin treatment (D). Ring spot total intensity and images were acquired 16 h after drug treatment (B), 72 h (C), or 1 wk (D) after transfection. Data were normalized to the ring spot total intensity of DMSO (B)-, siControl (C)-, or sgControl (D)-treated cells and represent the mean ± SEM (n = 3, from three independent experiments). Significance was calculated using one-way ANOVA with Tukey's test (B and C) or two-tailed Student's t test (D) with \*P < 0.05, \*\*P < 0.01, \*\*\*P < 0.001. n.s., not significant. Scale bar: 10 µm. (E) TauRD (P301L)-Venus aggregate-positive cells were transfected with control or TSG101 siRNA. Cells were lysed 72 h after transfection, and Triton X-100-soluble and Triton X-100-insoluble fractions were immunoprecipitated with a GST-tagged anti-GFP nanobody. Input and IP samples were immunoblotted with the indicated antibodies. Data were normalized to the band intensity of tauRD (P301L)-Venus or ubiquitin in lane 5 and represent the mean ± SEM (n = 3, from three independent experiments). Significance was calculated using one-way ANOVA with Tukey's test with \*P < 0.05, \*\*P < 0.01. n.s., not significant. (F) UbiCRest analysis of tauRD (P301L)-Venus ubiquitylation. TauRD (P301L)-Venus aggregate-positive cells were lysed, and the insoluble fraction was immunoprecipitated with a GST-tagged anti-GFP nanobody. 15  $\mu$ M K48-specific deubiquitinase OTUB1, 15  $\mu$ M K63-specific deubiquitinase AMSH-LP, or both were added to the immunoprecipitated samples and rotated at 37°C for 30 min and then immunoblotted with the indicated antibodies. Data were normalized to the band intensity of ubiquitin in the control sample and represent the mean  $\pm$  SEM (n = 3, from three independent experiments). Significance was calculated using one-way ANOVA with Dunnett's test with \*\*P < 0.01, \*\*\*P < 0.001. Source data are available for this figure: SourceData F3.

Fig. S4, C and D). The stable expression of full-length UBAP1 or TSG101 relieved this accumulation (Fig. 4, D and E, gray columns; and Fig. S4, C and D). Similarly, the stable expression of UBAP1 lacking the SOUBA domain (ΔSOUBA) relieved the accumulation caused by endogenous *UBAP1* KO (Fig. 4 D, white column, and Fig. S4 C). In contrast, under endogenous *TSG101* knockdown, cells expressing TSG101 lacking the UEV domain (ΔUEV) exhibited only partial reduction of tauRD (P301L) accumulation compared with cells expressing full-length TSG101 (Fig. 4 E, white column, and Fig. S4 D). Similarly, TSG101 (ΔUEV) showed remarkably reduced binding to ubiquitylated proteins compared with the full-length TSG101 (Fig. 4 F). These results suggest that the UEV domain in TSG101 is essential for endosomal microautophagy of ubiquitylated tauRD (P301L).

To confirm whether the UEV domain is required for the recognition of ubiquitylated tauRD (P301L) by ESCRT-I, we examined the colocalization between tauRD (P301L) aggregates and full-length and ubiquitin-binding domain-deleted forms of UBAP1 and TSG101. Colocalization between tauRD (P301L) aggregates and UBAP1 slightly but significantly decreased when the SOUBA domain of UBAP1 was absent (Fig. S4 E). In contrast, full-length TSG101 colocalized with tauRD (P301L) aggregates, whereas deletion of the UEV domain significantly reduced this colocalization (Fig. 4 G), demonstrating the importance of the UEV domain of TSG101 in recognizing ubiquitylated TauRD (P301L).

We further evaluated the importance of tauRD (P301L) ubiquitylation in substrate recognition. TAK-243 treatment significantly reduced the colocalization between tauRD (P301L) aggregates and TSG101 (Fig. 4 H). We also expressed doxycycline (Dox)-inducible tauRD (P301L), in which all lysine residues were mutated to arginine residues (tauRD (P301L/all-KR)), in tauRD (P301L) aggregate-positive cells. TauRD (P301L/all-KR) was detected in both Triton X-100-soluble and Triton X-100-insoluble fractions (Fig. S4 F, lanes 5-8). TauRD (P301L/all-KR) immunoprecipitated from these fractions was not ubiquitylated, as expected (Fig. S4 F, lanes 13-16, IB: Ub [Pan]). TSG101 knockdown did not lead to the accumulation of tauRD (P301L/all-KR), whereas it caused accumulation of tauRD (P301L) (Fig. S4 F). These results indicate that ubiquitylation of tauRD (P301L) is essential for its TSG101-dependent degradation.

### The bridge between ESCRT-I and ESCRT-III via PTPN23 is important for the clearance of tauRD (P301L)

We demonstrated that in addition to TSG101, the depletion of PTPN23, CHMP4A/B/C, and VPS4A/B caused enlargement of tauRD (P301L) aggregates (Fig. 3, C and D). PTPN23 has been shown to bind the ESCRT-I subunit UBAP1 via its coiled-coil (CC) domain, as revealed by the crystal structure of PTPN23-UBAP1 (Gahloth et al., 2016). Indeed, PTPN23 ( $\Delta$ CC) showed reduced binding to UBAP1 (Fig. 5, A and B). Furthermore, two residues (L202 and I206) in the Bro1 domain of PTPN23 are reported to be essential for its interaction with the ESCRT-III subunit CHMP4B (Doyotte et al., 2008). We observed that PTPN23 ( $\Delta$ Bro1) and PTPN23 (L202D/I206D) almost completely lost their ability to bind CHMP4B (Fig. 5, A and C), consistent with the result of an in vitro assay from a previous study (Doyotte et al., 2008).

To further examine the mechanistic role of PTPN23 in the endosomal microautophagy of tauRD (P301L), we stably expressed sgRNA-resistant variants of wild-type and the three mutant PTPN23 constructs (Fig. 5 A) in tauRD (P301L) aggregate-positive cells and knocked out endogenous PTPN23 using sgRNA. In the control mCherry-expressing cells, PTPN23 depletion caused a significant accumulation of tauRD (P301L), whereas wild-type PTPN23 expression alleviated this accumulation, consistent with the results in Fig. 1 K (Fig. 5 D and Fig. S5 A). In contrast, PTPN23 (ΔCC), PTPN23 (ΔBro1), and PTPN23 (L202D/I206D) expression failed to alleviate tauRD (P301L) accumulation under PTPN23 KO (Fig. 5 D and Fig. S5 A). These results demonstrate that PTPN23 binding to both ESCRT-I and ESCRT-III is essential for endosomal microautophagy of tauRD (P301L) and suggest that PTPN23 bridges ESCRT-I and ESCRT-III during this process.

### The UBAP1 mutant associated with HSP disrupts endosomal microautophagy of tauRD (P301L) aggregates

We demonstrated that the ESCRT-I subunit UBAP1 regulates tauRD (P301L) accumulation (Fig. 1, C and G) and that the PTPN23 mutant unable to bind UBAP1 disrupts tauRD (P301L) clearance (Fig. 5 D). These results underscore the critical role of UBAP1 in endosomal microautophagy.

Recent studies have identified UBAP1 mutations in patients with frontotemporal lobar degeneration (FTLD) and autosomal



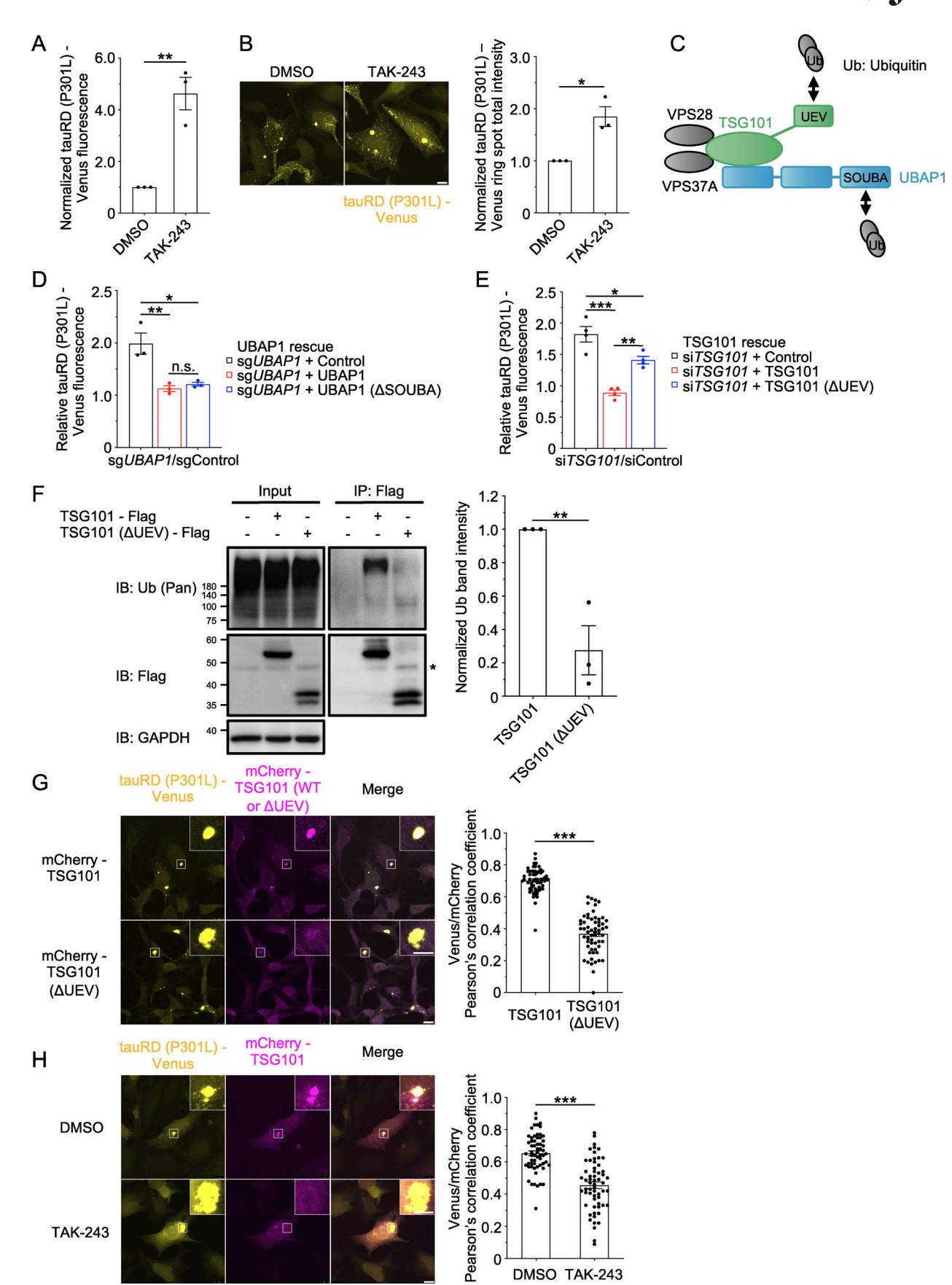


Figure 4. **UEV domain of TSG101 is necessary for its recognition of ubiquitylated tauRD (P301L). (A)** TauRD (P301L)-Venus aggregate–positive cells were treated with 100 nM TAK-243 for 24 h, and tauRD (P301L)-Venus fluorescence was measured by flow cytometry. Data were normalized to the Venus



fluorescence of DMSO-treated cells and represent the mean ± SEM (n = 3, from three independent experiments). Significance was calculated using two-tailed Student's t test with \*\*P < 0.01. (B) Ring spot total intensity of tauRD (P301L)-Venus aggregates was quantified by a high-content image analyzer; cells were imaged by a confocal microscope 16 h after treatment of 100 nM TAK-243. Data were normalized to the ring spot total intensity of DMSO-treated cells and represent the mean ± SEM (n = 3, from three independent experiments). Significance was calculated using two-tailed Student's t test with \*P < 0.05. Scale bar: 10 μm. (C) Schematic view of the ubiquitin-binding domains of the ESCRT-I complex. (D) TauRD (P301L)-Venus aggregate-positive cells stably expressing mCherry (control) or mCherry-tagged sgRNA-resistant variants of WT UBAP1 and UBAP1 (ΔSOUBA) were transfected with control or UBAP1 sgRNA, and successfully transfected cells were selected by puromycin selection. TauRD (P301L)-Venus fluorescence was measured by flow cytometry 1 wk after transfection. Data represent the Venus fluorescence from sgUBAP1-treated cells normalized to the Venus fluorescence from sgControl-treated cells. Data represent the mean ± SEM (n = 3, from three independent experiments). Significance was calculated using one-way ANOVA with Tukey's test with \*P < 0.05, \*\*P < 0.01. n.s., not significant. (E) TauRD (P301L)-Venus aggregate-positive cells stably expressing mCherry (control) or mCherry-tagged siRNA-resistant variants of WT TSG101 and TSG101 (ΔUEV) were transfected with control or TSG101 siRNA. TauRD (P301L)-Venus fluorescence was measured by flow cytometry 72 h after transfection. Data represent the Venus fluorescence from siTSG101-treated cells normalized to the Venus fluorescence from siControltreated cells. Data represent the mean ± SEM (n = 4, from four independent experiments). Significance was calculated using one-way ANOVA with Tukey's test with \*P < 0.05, \*\*P < 0.01, \*\*\*P < 0.001. (F) TSG101 recognizes ubiquity lated proteins via the UEV domain. HEK293T cells were transfected with TSG101-Flag, TSG101 (ΔUEV)-Flag, and empty vector. Cells were lysed 48 h after transfection, and TSG101-Flag and TSG101 (ΔUEV)-Flag were immunoprecipitated. Input and IP samples were immunoblotted with the indicated antibodies. Data were normalized to the band intensity of ubiquitin in TSG101 immunoprecipitated samples and represent the mean  $\pm$  SEM (n = 3, from three independent experiments). Significance was calculated using two-tailed Student's t test with \*\*P < 0.01. The asterisk denotes a nonspecific band. (G) Visualization of tauRD (P301L)-Venus aggregates and TSG101 and TSG101 (ΔUEV) in cells stably expressing mCherry-tagged WT TSG101 and TSG101 (ΔUEV). Endogenous TSG101 was depleted by siRNA knockdown. Images were acquired by a confocal microscope, and boxed areas are magnified at the top right corner. Pixel intensity correlation of tauRD (P301L)-Venus aggregates was calculated. Data represent the mean ± SEM (n = 60, from three independent experiments, 20 cells per experiment). Significance was calculated using two-tailed Student's t test with \*\*\*P < 0.001. Scale bar: 10 and 5 µm (magnified images). (H) Visualization of tauRD (P301L)-Venus aggregates and TSG101 in tauRD (P301L)-Venus aggregate-positive cells stably expressing Tet-On mCherry-TSG101. After treating cells with 100 nM TAK-243 for 16 h, 1 µl/ml Dox was added, and cells were incubated for an additional 8 h. Images were acquired by a confocal microscope, and boxed areas are magnified at the top right corner. Pixel intensity correlation of tauRD (P301L)-Venus aggregates was calculated. Data represent the mean ± SEM (n = 60, from three independent experiments, 20 cells per experiment). Significance was calculated using two-tailed Student's t test with \*\*\*P < 0.001. Scale bar: 10 and 5 µm (magnified images). Source data are available for this figure: SourceData F4.

dominant HSP (Nan et al., 2019; Wang et al., 2020; Lin et al., 2019; Farazi Fard et al., 2019; Gu et al., 2020; Bourinaris et al., 2020; Rollinson et al., 2009). Since previous studies have reported tau pathology in patients with these diseases (Rossi and Tagliavini, 2015; Wharton et al., 2003), we examined the FTLD mutant S391Afs21X and the HSP mutant p.K143Sfs\*15 (Fig. 6 A) to investigate the physiological significance of ESCRT-mediated endosomal microautophagy in tau aggregate clearance.

We stably expressed sgRNA-resistant variants of wild-type UBAP1 and FTLD and HSP mutants in tauRD (P301L) aggregate-positive cells. To confirm the effect of each UBAP1 construct, we knocked out endogenous UBAP1 in each cell line and evaluated its impact on tauRD (P301L) accumulation. In control mCherry-expressing cells, UBAP1 deletion caused tauRD (P301L) accumulation (Fig. 6 B and Fig. S5 B), consistent with the results in Fig. 1 H. UBAP1 KO in cells stably expressing full-length UBAP1 or UBAP1 (S391Afs21X) alleviated this accumulation (Fig. 6 B and Fig. S5 B). In contrast, the expression of UBAP1 (p.K143Sfs\*15) failed to alleviate the accumulation of tauRD (P301L) upon KO of UBAP1 (Fig. 6 B and Fig. S5 B).

UBAP1 (S391Afs21X) exhibits premature termination, resulting in a partial loss of the SOUBA domain (Fig. 6 A). On the other hand, in UBAP1 (p.K143Sfs\*15), a two-nucleotide deletion causes a frameshift, resulting in the loss of both the SOUBA and the PBR domain while preserving only the UBAP1-MVB12-associated (UMA) domain (Fig. 6 A) (Gahloth et al., 2016). The UMA domain is responsible for the incorporation of UBAP1 into the ESCRT-I complex (Gahloth et al., 2016). These results raise the possibility that the PBR domain, rather than the SOUBA domain, is required for clearance of tauRD (P301L). Therefore, in addition to UBAP1 (ΔSOUBA), we generated UBAP1 lacking the PBR domain (ΔPBR) to test its importance (Fig. 6 A). Indeed, PTPN23 was co-immunoprecipitated with full-length UBAP1 and

UBAP1 (ΔSOUBA), whereas UBAP1 (ΔPBR) showed reduced coimmunoprecipitation with PTPN23 (Fig. 6 C), confirming that PTPN23 binds to the PBR domain in UBAP1 (Gahloth et al., 2017). The expression of UBAP1 (ΔPBR) failed to alleviate the accumulation of tauRD (P301L) following KO of endogenous UBAP1, whereas the expression of UBAP1 (ΔSOUBA) alleviated it (Fig. 6 B and Fig. S5 B). Furthermore, UBAP1 (p.K143Sfs\*15) and UBAP1 (ΔPBR) expression resulted in significant enlargement of tauRD (P301L) aggregates (Fig. 6 D), consistent with the results of lysosome and the ESCRT machinery inhibition (Fig. 3, B-D). In contrast, the expression of UBAP1, UBAP1 (S391Afs21X), or UBAP1 (ΔSOUBA) did not alter the size of tauRD (P301L) aggregates (Fig. 6 D). These results suggest that the recruitment of PTPN23 via the PBR domain in UBAP1 is essential for ESCRTmediated endosomal microautophagy of tauRD (P301L) aggregates and that loss of the PBR domain in UBAP1 may impair the clearance of tau aggregates, leading to their accumulation in HSP.

### ESCRT-mediated endosomal microautophagy also targets full-length tau (P301L) in SH-SY5Y cells

To examine whether ESCRT-mediated endosomal micro-autophagy is responsible for the degradation of full-length tau, we established a human neuroblastoma-derived SH-SY5Y cell line stably expressing the 2N4R isoform of full-length tau (P301L) (tauFL [P301L]) tagged with Venus (Fig. S1 A). We then seeded the cells with sarkosyl-insoluble extracts prepared from tauRD (P301L) aggregate-positive HEK293A cells, thereby establishing an SH-SY5Y cell line stably propagating tauFL (P301L) aggregates (Fig. 7 A). We observed that KO of TSGI01 and PTPN23 resulted in a significant accumulation of tauFL (P301L) (Fig. 7, B and C). CHMP4B KO increased the accumulation of tauFL (P301L), although the increase was not statistically significant



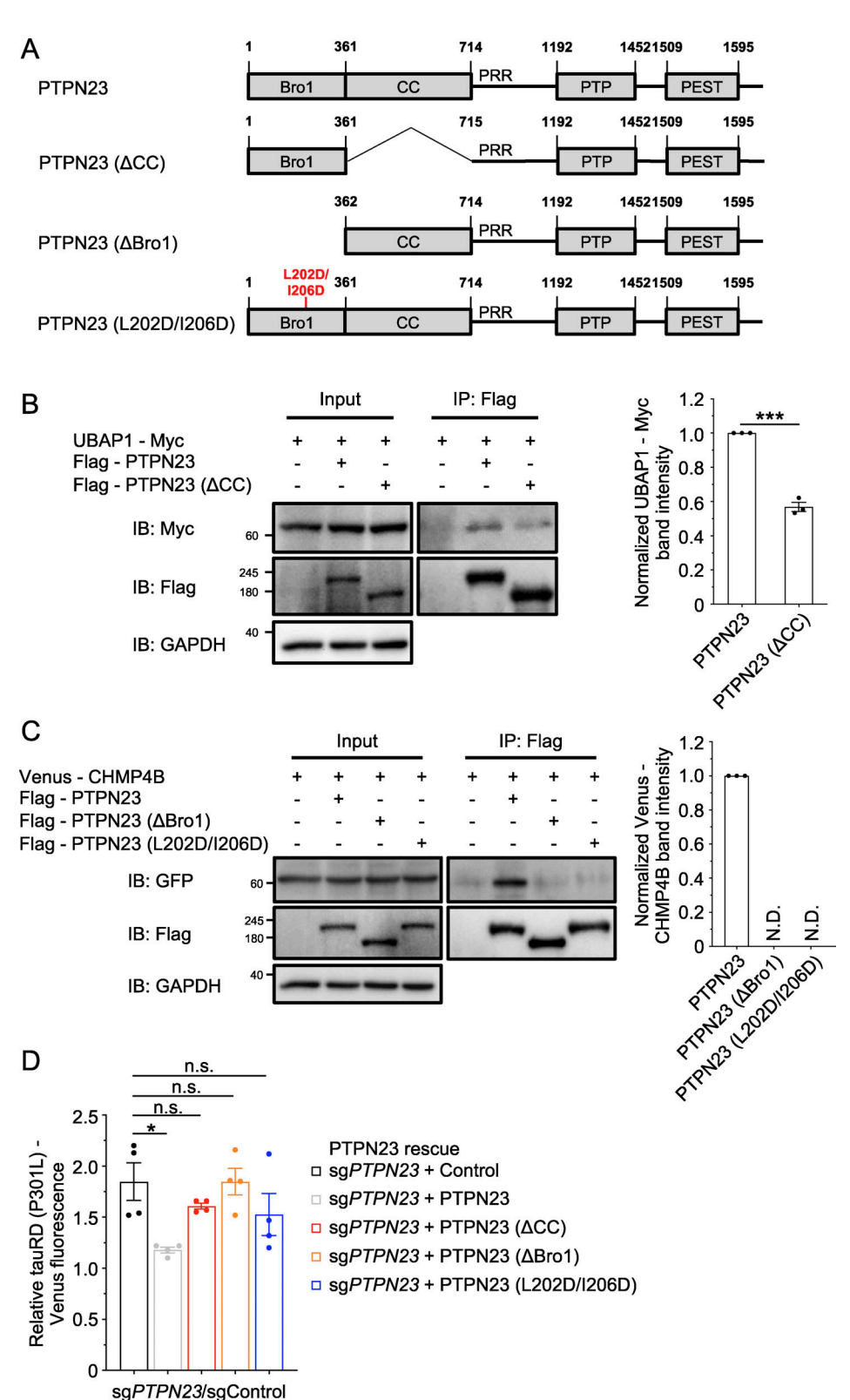


Figure 5. PTPN23 bridges ESCRT-II and ESCRT-III, completing lysosomal degradation of tauRD (P301L). (A) Schematic view of WT PTPN23 and its mutants. (B) PTPN23 binds to UBAP1 via the CC domain. HEK293T cells were transfected with UBAP1-Myc, Flag-PTPN23, Flag-PTPN23 (ΔCC), and empty vector. Cells were lysed 48 h after transfection, and Flag-PTPN23 proteins were immunoprecipitated. Input and IP samples were immunoblotted with the indicated antibodies. Data were normalized to the band intensity of UBAP1-Myc in PTPN23 immunoprecipitated samples and represent the mean ± SEM (n = 3, from three independent experiments). Significance was calculated using two-tailed Student's t test with \*\*\*P < 0.001. (C) PTPN23 binds to CHMP4B via residues L202 and I206 in the Bro1 domain. HEK293T cells were transfected with Venus-CHMP4B, Flag-PTPN23, Flag-PTPN23 (\Delta Bro1), Flag-PTPN23 (L202D/ 1206D), and empty vector. Cells were lysed 48 h after transfection, and Flag-PTPN23 proteins were immunoprecipitated. Input and IP samples were

Men et al. Journal of Cell Biology Microautophagy of tau aggregates



immunoblotted with the indicated antibodies. Data were normalized to the band intensity of Venus-CHMP4B in PTPN23 immunoprecipitated samples and represent the mean  $\pm$  SEM (n=3, from three independent experiments). N.D., not detected. **(D)** TauRD (P301L)-Venus aggregate-positive cells stably expressing mCherry (control) or mCherry-tagged sgRNA-resistant PTPN23 proteins illustrated in A were transfected with control or *PTPN23* sgRNA, and successfully transfected cells were selected by puromycin selection. TauRD (P301L)-Venus fluorescence was measured by flow cytometer 1 wk after transfection. Data represent the Venus fluorescence from sgPTPN23-treated cells normalized against the Venus fluorescence from sgControl-treated cells. Data represent the mean  $\pm$  SEM (n=4, from four independent experiments). Significance was calculated using one-way ANOVA with Dunnett's test with \*P < 0.05. *n.s.*, not significant. Source data are available for this figure: SourceData F5.

(Fig. 7, B and C). We also observed that depletion of the proteasome subunit PSMA6 (α1) and VCP caused a significant accumulation of tauFL (P301L), whereas KO of the macroautophagy factors ATG7 and FIP200 or the CMA protein LAMP2 did not (Fig. 7, B and C). Treatment with TAK-243 caused a significant accumulation of tauFL (P301L) (Fig. 7 D), indicating that ubiquitylation is essential for the clearance of tauFL (P301L) aggregates. Biochemical characterization of tauFL (P301L) revealed that KO of either TSG101 or PTPN23 markedly increased the amount of Triton X-100-insoluble tauFL (P301L) ubiquitylated in SH-SY5Y cells (Fig. 7 E, 10–12). These findings closely mirror those observed in HEK293A cells (Fig. 1 C, Fig. SI, H and I, Fig. 3 E, and Fig. 4 A), suggesting that ESCRT-mediated endosomal microautophagy represents a conserved mechanism for the clearance of tau aggregates.

#### Discussion

It had remained unclear whether microautophagy is involved in the degradation of protein aggregates and which molecules are involved in macroautophagic degradation of protein aggregates. In this study, we used cell models stably expressing tauRD (P301L) and tauFL (P301L) aggregates to demonstrate that the endosomal microautophagy of tau aggregates is mediated by UBAP1-containing ESCRT-I, PTPN23, and ESCRT-III. We termed this process as microaggrephagy.

We demonstrated that ESCRT-I recognizes ubiquitylated tau aggregates through the UEV domain in TSG101 and recruits the accessory factor PTPN23 via the PBR domain in UBAP1 (Fig. 7 E). PTPN23 and its paralog Alix are both Bro1 domain-related proteins that perform functions analogous to those of ESCRT-II by recruiting and activating ESCRT-III (Parkinson et al., 2015; Tang et al., 2016; Ichioka et al., 2007). However, only PTPN23, but not Alix, binds UBAP1 (Gahloth et al., 2017). Indeed, our genomewide CRISPR KO screen did not identify Alix as a regulatory factor in the clearance of aggregated tauRD (P301L). These observations suggest that the UBAP1-PTPN23 association is specific and essential for microaggrephagy of ubiquitylated tau aggregates. This is consistent with our results, which demonstrated that the expression of a PTPN23 mutant with the UBAP1 binding region deleted ( $\Delta$ CC) and a UBAP1 mutant lacking the PTPN23 binding domain (ΔPBR) caused a defect in the clearance of tauRD (P301L) aggregates (Fig. 5 D and Fig. 6 B). Although PTPN23 ( $\triangle$ CC) is a loss-of-function mutant, it did not completely abolish interaction with UBAP1 (Fig. 5 B). Improper folding of PTPN23 upon CC domain deletion may create nonspecific interactions with UBAP1. Therefore, future studies are needed to clarify the amino acid residues responsible for the interaction between UBAP1 and PTPN23 using mammalian cells, and

Microautophagy of tau aggregates

PTPN23 carrying point mutations in such residues is helpful to further corroborate our domain deletion results.

Alix associates with protein aggregates via a distinct pathway and is well known for its role in sorting and secreting exosomes, which are thought to play a key role in the prion-like propagation of protein aggregates containing cross- $\beta$  sheets in neurodegenerative diseases (Polanco and Götz, 2022; Cone et al., 2020; Baietti et al., 2012; Natale et al., 2022; Ghossoub et al., 2014). In contrast, we demonstrated that PTPN23 is involved in the microautophagy of tau aggregates. The molecular mechanism underlying the differential sorting of ubiquitylated tau aggregates into the Alix- or PTPN23-dependent pathways remains unclear. Further studies are needed to understand the sorting mechanism underlying the propagation and degradation of amyloidogenic protein aggregates.

A recent study reported that dysfunction of the ESCRT pathway promotes the propagation of tau aggregates taken up from the extracellular space (Chen et al., 2019). Specifically, the authors identified CHMP6, a subunit of the ESCRT-III complex, through CRISPRi screening for regulators of endocytosed tau aggregates and found that CHMP6 knockdown significantly increased tau propagation. ESCRT-III is known to play a role in repairing endolysosomal membranes (Skowyra et al., 2018). Indeed, they revealed that dysfunction of ESCRT-III caused endolysosomal damage, which subsequently promoted the intracellular propagation of endocytosed tau aggregates. However, our findings suggest that this mechanism does not play a primary role in our model (Fig. S3, B-E). In the previous study, the authors added recombinant tau seeds or patient brain-derived extracts externally into their tau-expressing cells in each experiment (Chen et al., 2019). In contrast, we did not add recombinant tau fibrils in any experiment after establishing the tauRD (P301L) aggregate-positive cell line, and the amount of tau aggregates secreted in our model was extremely limited (Fig. S3 B). As these two studies were performed under different conditions, this likely explains the observed discrepancy.

Studies using Neuro2a and DAOY cells have shown that both macroautophagy and endosomal microautophagy contribute to tau clearance (Vaz-Silva et al., 2018; Benyair et al., 2023). Furthermore, reports suggest that tau degradation via microautophagy is comparable to macroautophagy (Caballero et al., 2021). However, these studies focused on soluble tau and did not address whether microautophagy targets tau aggregates or investigate the cargo transfer mechanisms from substrate recognition to lysosomal degradation of ubiquitylated protein aggregates.

Recent studies have linked the ESCRT-I subunit UBAP1 to neurological diseases, including FTLD and HSP (Nan et al., 2019; Wang et al., 2020; Lin et al., 2019; Farazi Fard et al., 2019; Gu



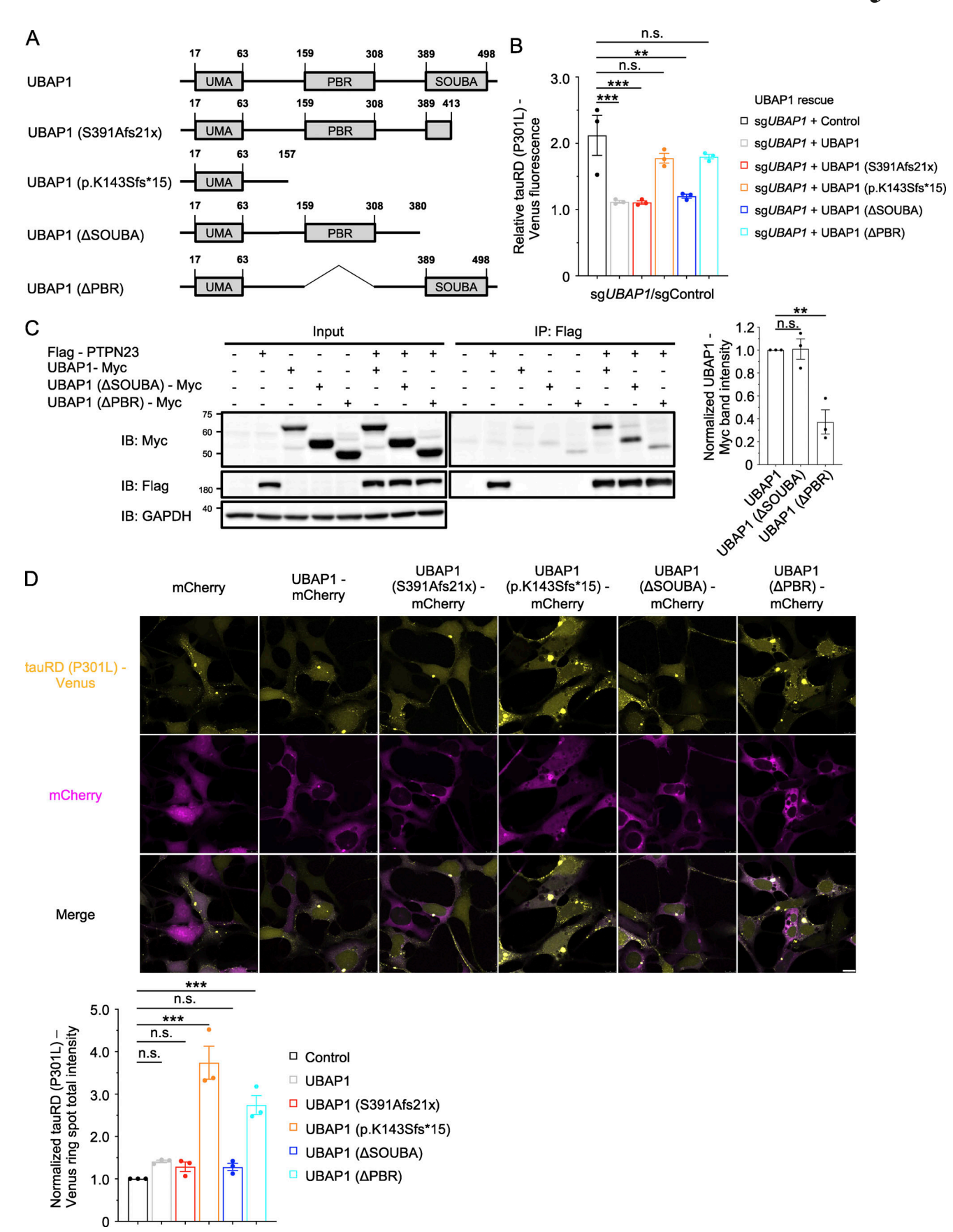


Figure 6. HSP-associated UBAP1 disrupts tauRD (P301L) clearance. (A) Schematic view of WT UBAP1 and its mutants. (B) TauRD (P301L)-Venus aggregate-positive cells stably expressing mCherry (control) or mCherry-tagged sgRNA-resistant WT UBAP1 and its mutants illustrated in A were transfected



with control or *UBAP1* sgRNA, and successfully transfected cells were selected by puromycin. TauRD (P301L)-Venus fluorescence was measured by flow cytometer 1 wk after transfection. Data represent the Venus fluorescence from sg*UBAP1*-treated cells normalized against the Venus fluorescence from sgControl-treated cells. Data represent the mean  $\pm$  SEM (n = 3, from three independent experiments). Significance was calculated using one-way ANOVA with Dunnett's test with \*\*P < 0.01, \*\*\*P < 0.001, n.s., not significant. (*C*) UBAP1 binds to PTPN23 via the PBR domain. HEK293T cells were transfected with Flag-PTPN23, UBAP1-Myc, UBAP1 ( $\Delta$ SOUBA)-Myc, UBAP1 ( $\Delta$ PBR)-Myc, and empty vector. Cells were lysed 48 h after transfection, and Flag-PTPN23 was immunoprecipitated. Input and IP samples were immunoblotted with the indicated antibodies. Data were normalized to the band intensity of UBAP1-Myc in PTPN23 immunoprecipitated samples and represent the mean  $\pm$  SEM (n = 3, from three independent experiments). Significance was calculated using one-way ANOVA with Dunnett's test with \*\*P < 0.01. n.s. not significant. (*D*) Ring spot total intensity of tauRD (P301L)-Venus aggregates in cells stably expressing mCherry (Control) or mCherry-tagged WT UBAP1 and its mutants illustrated in A was quantified by a high-content image analyzer, and cells were imaged by a confocal microscope. Data were normalized to the ring spot total intensity of mCherry (control) cells and represent the mean  $\pm$  SEM (n = 3). Significance was calculated using one-way ANOVA with Dunnett's test with \*\*\*P < 0.001. n.s., not significant. Scale bar: 10  $\mu$ m. Source data are available for this figure: SourceData F6.

et al., 2020; Bourinaris et al., 2020; Rollinson et al., 2009). We found that the ectopic expression of the HSP variant UBAP1 (p.K143Sfs\*15) lacking both the SOUBA and the PBR domain, but not the FTLD variant UBAP1 (S391Afs21X), resulted in a significant enlargement of tauRD (P301L) aggregates (Fig. 6 D). Our results suggest that the PBR, rather than the SOUBA domain, is crucial for ESCRT-mediated microaggrephagy (Fig. 6, B-D). These findings provide insight into the mechanism by which UBAP1 (p.K143Sfs\*15) is involved in the pathogenesis of HSP. Interestingly, tau pathology has also been observed in HSP patients (Wharton et al., 2003), suggesting a potential link between tau and HSP. Further research is needed to elucidate the physiological links between microaggrephagy, tau, and HSP.

In this study, we demonstrated that aggregated tau is a substrate for ESCRT-mediated microaggrephagy. An important question remains whether other protein aggregates associated with neurodegenerative diseases are also targeted by this pathway. To address this, we generated HEK293A cell lines expressing either α-synuclein (α-Syn) (A53T) aggregates, a Parkinson's disease-associated mutation, or polyglutamine 97 (PolyQ97) aggregates, which is associated with Huntington's disease. Interestingly, the depletion of TSG101, PTPN23, CHMP4A/B/C, and VPS4A/B caused significant accumulation of α-Syn (A53T) (Fig. S5, C-E). In contrast, PolyQ97 showed only minor or no changes under the same conditions (Fig. S5, F-H). The reason for this substrate selectivity remains unclear, and future studies are required to elucidate the mechanisms by which certain protein aggregates are targeted by ESCRTmediated microaggrephagy, while others are not. Crossβ-sheet-containing misfolded protein aggregates, including tau and  $\alpha$ -Syn, possess distinctive features in terms of localization, posttranslational modification, and cross-β-sheet structure (Uemura et al., 2020; Kyalu Ngoie Zola et al., 2023; Kametani et al., 2024). In this study, we used frontotemporal dementia mutant tau (P301L). However, it has been reported that the cross- $\beta$ -sheet structure of tau (P301L) aggregates differs from that of wild-type tau aggregates in sporadic Alzheimer's disease (Strang et al., 2018). A single polypeptide chain can also adopt multiple fibril states across various neurodegenerative diseases, a phenomenon known as structural polymorphism (Wilkinson et al., 2023; Fändrich et al., 2018). Expanding the generalizability of this study will require further investigations into other types of protein aggregates, such as wild-type tau and amyloid-β. It is also an intriguing question whether other

Microautophagy of tau aggregates

macromolecular condensates, such as ferritin droplets, are degraded by the same mechanism. A previous study showed that ferritin lysosomal turnover is independent of macro-autophagy and regulated by ESCRT proteins, including VPS37A (ESCRT-I subunit), PTPN23, and CHMP4B (ESCRT-III subunit) (Goodwin et al., 2017). This study raises the possibility that the microaggrephagy mechanism proposed in this work may also target ferritin droplets. Since macromolecular condensates share certain features with protein aggregates, they may represent potential targets for the microaggrephagy pathway. Future studies should focus on gaining a deeper understanding of microaggrephagy substrates.

### **Materials and methods**

### **Expression vectors**

Human tauRD (residues 244-372 in the 2N4R tau isoform) and 2N4R isoform of full-length tau cDNAs were cloned from pRK172-Tau 2N4R (a gift from Dr. T. Miyasaka, Department of Physiology and Anatomy, Nihon University School of Pharmacy, Funabashi, Japan) (Saito et al., 2021). Human α-Syn cDNA was amplified from the cDNA of hTERT-RPE1 cells by PCR. Human polyglutamine 97 cDNA was described previously (Nakajima et al., 1996). Human cDNAs encoding TSG101, UBAP1, VPS28, VPS37A, PTPN23, and CHMP4B were amplified from the cDNA of A549 or HEK293T cells by PCR. Human Rab5A (Q79L) cDNA was cloned from pBABEpuro 3xFlag-Rab5A (Q79L), and human Rab7A (Q67L) cDNA was cloned from pcDNA3.1 3xFlag-TEV-Rab7A (Q67L) (gifts from Dr. K. Yamano, Department of Biomolecular Pathogenesis, Medical Research Institute, Tokyo Medical and Dental University (TMDU) (Medical Research Laboratory, of Integrated Research, Institute of Science Tokyo), Bunkyo City, Japan). pGEX-6P-1 GFP-Nanobody was a gift from Dr. K. Nakayama, Department of Physiological Chemistry, Graduate School of Pharmaceutical Sciences, Kyoto University, Kyoto, Japan (plasmid #61838; Addgene). Point mutations and domain deletions were introduced using PrimeSTAR Mutagenesis Basal Kit (Takara) according to the manufacturer's protocol and confirmed by sequencing (Genewiz). All plasmids used in this study are listed in Table S1.

### Cell culture and drug treatment

HEK293A (Thermo Fisher Scientific) and HEK293T (American Type Culture Collection [ATCC]) cells were cultured in



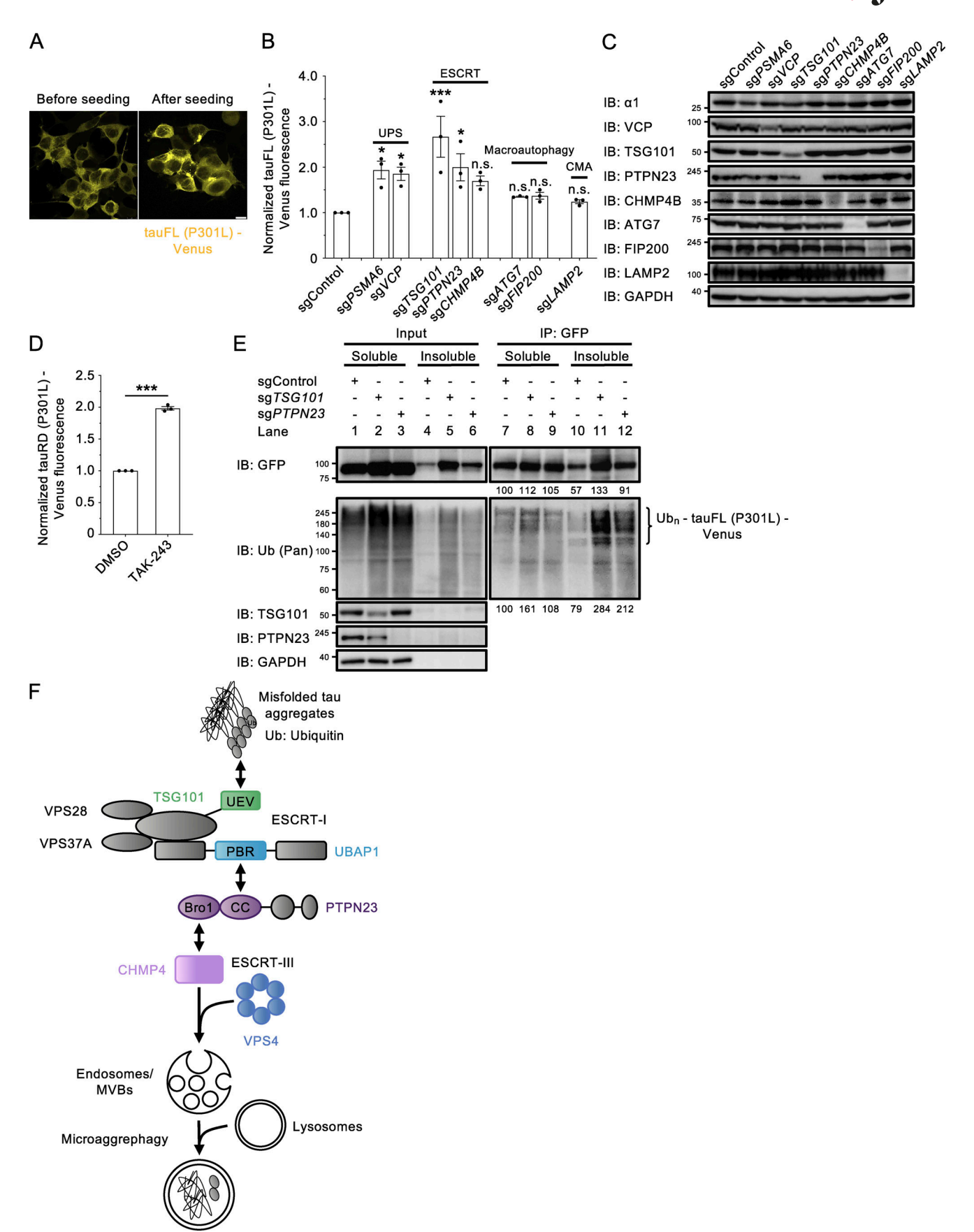


Figure 7. **ESCRT-mediated microaggrephagy targets tauFL (P301L) in SH-SY5Y cells. (A)** Representative image of tauFL (P301L)-Venus aggregate-positive SH-SY5Y cells before and after seeding. Images were acquired by a confocal microscope. Scale bar: 10 μm. **(B and C)** TauFL (P301L)-Venus



aggregate–positive SH-SY5Y cells were transfected with control or individual sgRNA, as indicated, and successfully transfected cells were selected by puromycin. TauFL (P301L)-Venus fluorescence was measured by flow cytometer (B), and whole-cell lysates were immunoblotted with the indicated antibodies (C) 1 wk after transfection. Data were normalized to the Venus fluorescence of sgControl-treated cells and represent the mean ± SEM (n = 3, from three independent experiments). Significance was calculated using one-way ANOVA with Dunnett's test with \*P < 0.05, \*\*\*P < 0.001. n.s., not significant. (D) TauFL (P301L)-Venus aggregate–positive SH-SY5Y cells were treated with 500 nM TAK-243 for 20 h, and tauFL (P301L)-Venus fluorescence was measured by flow cytometry. Data were normalized to the Venus fluorescence of DMSO-treated cells and represent the mean ± SEM (n = 3, from three independent experiments). Significance was calculated using two-tailed Student's t test with \*\*\*P < 0.001. (E) TauFL (P301L)-Venus aggregate–positive SH-SY5Y cells were transfected with control, TSG101, or PTPN23 sgRNA, and successfully transfected cells were selected by puromycin. Cells were lysed 1 wk after transfection, and Triton X-100–soluble and Triton X-100–insoluble fractions were immunoprecipitated with a GST-tagged anti-GFP nanobody. Input and IP samples were immunoblotted with the indicated antibodies. Data were normalized to the band intensity of tauFL (P301L)-Venus or ubiquitin in lane 7. (F) The ESCRT-I complex binds to ubiquitylated tau aggregates via the UEV domain in TSG101. The CC domain in PTPN23 interacts with the PBR domain in the ESCRT-I subunit UBAP1. The ESCRT-III subunit CHMP4 is recruited to PTPN23 via its Bro1 domain. ESCRT-III then recruits the AAA ATPase VPS4 to complete the endosomal microautophagy of tau aggregates. Source data are available for this figure: SourceData F7.

Dulbecco's modified Eagle's medium (DMEM) (Nacalai Tesque) supplemented with 5% heat-inactivated fetal bovine serum (Thermo Fisher Scientific), 100 U/ml penicillin (Nacalai Tesque), and 100 μg/ml streptomycin (Nacalai Tesque) at 37°C with 5% CO<sub>2</sub>. SH-SY5Y (ATCC) cells were cultured in a 1: 1 mixture of DMEM and Ham's F12 (048-29785; FUJIFILM Wako Pure Chemical Corporation) supplemented with 15% heat-inactivated fetal bovine serum (Thermo Fisher Scientific), 100 U/ml penicillin (Nacalai Tesque), 100 μg/ml streptomycin (Nacalai Tesque), and 1% nonessential amino acids (Gibco Life Technologies) at 37°C with 5% CO<sub>2</sub>. Cells were treated with BTZ (LC Laboratories), BafA1 (Santa Cruz Biotechnology), E64d (Roche), pepstatin A (Roche), Dox (Sigma Millipore), or TAK-243 (Active Biochem) at the indicated concentrations and times.

### **Transfection**

Transient transfection was performed using polyethylenimine (PEI) MAX (MW: 40,000) (Tokyo Chemical Industry) according to the manufacturer's protocol. Transfections were performed for 48–72 h prior to cell analysis. siRNA-mediated knockdown experiments were performed using Lipofectamine RNAiMAX (Thermo Fisher Scientific) according to the manufacturer's protocol. Transfections were performed for 72–96 h prior to cell analysis. The siRNA sequences (Horizon Cell Discovery) are as follows:

Control (Nanoluc), 5'-CCUGUGGAACGGCAACAAA-3' TSG101, 5'-CCUCCAGUCUUCUCUCGUC-3'.

CHMP4A (L-020698-01; SMART pool):

J-020698-09: 5'-GGCACAAACUGACGGGACA-3' J-020698-10: 5'-UGUUAAAUGUGGGCGACAA-3' J-020698-11: 5'-GGAAGAAAAGAUUCGAACA-3' J-020698-12: 5'-CCCUGGAGUUUCAGCGUGA-3'.

CHMP4B (L-018075-01; SMART pool):

J-018075-09: 5'-CCAUCGAGUUCCAGCGGGA-3' J-018075-10: 5'-AGAAGAGUUUGACGAGGAU-3' J-018075-11: 5'-CGGAAGAGAUGUUAAGCAA-3' J-018075-12: 5'-UGGAAAGGGUCGACUGGUU-3'

CHMP4C (L-015932-01; SMART pool):

J-015932-09: 5'-UGUUAUUUCCUAUGCGAAU-3' J-015932-010: 5'-GCAGCUUGGGCUACCUAAA-3' J-015932-011: 5'-GGAUAUCGCCCAAGAAAUC-3' J-015932-012: 5'-AAGCACGGCACGCAGAAUA-3' VPS4A: 5'-GAGCCAAGUGCGUGCAGUA-3' VPS4B: 5'-GGAUGUCCCUGGAGAUAAA-3'.

sgRNA-mediated KO experiments were performed using lentiCRISPR v2 and PEI-MAX. Successful incorporation was selected for using DMEM containing 2  $\mu$ g/ml puromycin at 24 h after transfection for 24 h, and cells were analyzed 1 wk after transfection. sgRNA sequences were obtained from Toronto KnockOut CRISPR Library—Version 3 (TKOv3) and cloned into lentiCRISPR v2. The sgRNA sequences are as follows:

Control sgRNA: 5'-CTGAAAAAGGAAGGAGTTGA-3' sgPSMA6: 5'-GCATACTTACAACAACCAAG-3' sgPSMD7: 5'-TACAGAAGCGTACATTTCAG-3' sgVCP: 5'-CAACAATTAACCGATTGGGA-3' sgHRS: 5'-GAACGAGCCCAAGTACAAGG-3' sgSTAM: 5'-GGAGCATGTGTATCAAACTG-3' sgTSG101: 5'-ATAGGACGAGAGAAGACTGG-3' sgUBAP1: 5'-ATTGGACAATAACTTGCCCA-3' sgVPS28: 5'-GAAGTTGTACAAGAACGCCC-3' sgVPS37A: 5'-GAGGAGGCGCTCTTGGTCAG-3' sgPTPN23: 5'-GATCTGGCTGGACCTGAAGG-3' sgVPS22: 5'-CTGGCGCTGAAGCATCGGAA-3' sgVPS25: 5'-GGTGGGAAGCGATACTGCCA-3' sgVPS36: 5'-GGTGCGAATCTACGATGGCG-3' sgCHMP1A: 5'-GGCGGAGAAGGACTCCAAGG-3' sgCHMP4B: 5'-GTTTGGAGAAGAGTTTGACG-3' sgCHMP5: 5'-GATGAGAGAGGGTCCTGCAA-3' sgCHMP6: 5'-TCAGGGTGCCACCTACCCGC-3' sgATG7: 5'-TGTAACTTAGCCCAGTACCC-3' sgFIP200: 5'-TGAAGATCGGCTCTACGCCC-3' sgLAMP2: 5'-ACTGTAACCATTTCAGACCA-3'.

#### qRT-PCR

Total RNA was isolated from cultured cells using a High Pure RNA isolation kit (Roche) and reverse-transcribed to cDNA with ReverTra Ace qPCR RT Master Mix (Toyobo). CHMP4A gene levels were measured by qPCR using THUNDERBIRD Probe qPCR Mix (Toyobo), a Universal ProbeLibrary probe (Roche), and a LightCycler 480 system (Roche). The CHMP4A gene level was normalized to GUSB mRNA levels. Real-time PCR data were analyzed by the  $\Delta\Delta$ CT method. PCR primer sequences are as



follows: CHMP4A, 5'-TGCCACTACCAATGCAGAAGT-3' and 5'-CCATGTCCTGGTAGGCCTTC-3', and GUSB, 5'-CGCCCTGCCTAT CTGTATTC-3' and 5'-TCCCCACAGGGAGTGTGTAG-3'. Probe numbers are as follows: CHMP4A (#44) and GUSB (#57).

### Stable cell line generation

To generate stable cell lines, cells were selected with either 0.4–4.0 μg/ml puromycin or 0.8 mg/ml G418. Alternatively, stable cell lines were established through lentiviral transduction and cell sorting using a SH800S cell sorter (SONY). HEK293T cells were transfected with CSII-EF-MCS (RDB04378; RIKEN BioResource Center, Kyoto, Japan)-based plasmids containing the cDNA of interest, a packaging plasmid (pCAG-HIVgp; RDB04394; RIKEN BioResource Center), and a VSV-G- and Revexpressing plasmid (pCMV-VSV-G-RSV-Rev; RDB04393; RIKEN BioResource Center) to produce lentiviruses. Supernatants were collected at 96 h after transfection, and cells were cultured with the supernatants for 48 h.

### CRISPR-based genome-wide screen

The TKOv3 was a gift from Dr. J. Moffat, Institute of Biomedical Engineering, University of Toronto, Toronto, Canada (#90294; Addgene). TKOv3 containing 4 types of sgRNA with different sequences per gene was used to perform genome-wide CRISPR KO screen (Hart et al., 2017). TKOv3 was introduced and amplified by electroporation into Endura electrocompetent cells (Lucigen) (Fig. 1 A). TKOv3 was transduced into  $9 \times 10^7$  tauRD (P301L)-Venus aggregate-positive HEK293A cells by lentivirus, and selection was performed using 2 µg/ml puromycin for 24 h. The multiplicity of infection was measured 4 days after the viral infection and was found to be 0.32. Infected cells were divided into triplicates. Fluorescence intensity of tauRD (P301L)-Venus was measured using a SH800S cell sorter (SONY) 1 wk after virus infection, and cells in the top 20% were sorted for each of the triplicates. Genomic DNA was extracted from the obtained cells, and a region of about 260 bp around the sgRNA was amplified by two-step PCR according to a previous study (Joung et al., 2017) (Fig. 1 A). The sequence of the sgRNA in the obtained PCR product was identified by next-generation sequencing using HiSeq 2500 (Illumina). The  $\beta$ -score and P value were calculated by MAGeCK-VISPR (Li et al., 2015), and the genes with the top 500  $\beta$ -scores and a P value of 0.05 or less were identified as hits.

### Preparation of recombinant tauRD and α-Syn fibrils

The gene encoding the wild-type tauRD and the gene encoding the wild-type  $\alpha\textsc{-Syn}$  were cloned into a pGEX-6P-1 vector, which was induced with 0.3 mM isopropyl  $\beta\textsc{-D-1-thiogalactopyranoside}$  (IPTG) at 37°C for 6 h. Cells were lysed in lysis buffer (1% Nonidet P-40, 1 mM EDTA in PBS) supplemented with cOmplete Mini EDTA-free protease inhibitor cocktail (Roche) followed by sonication (10 min, output = 4, duty = 30). Cell lysates were clarified by centrifugation at 10,000 rpm for 20 min before application onto glutathione Sepharose 4B resin (GE Healthcare). Resin was washed twice with Milli-Q water followed by one wash with lysis buffer prior to protein elution with GSH elution buffer (50 mM Tris, pH 8.0, 10 mM GSH). Eluted protein

was quantified by the Bradford assay (Nacalai Tesque) and diluted to 2.4  $\mu$ M with GSH elution buffer. 1 mM DTT, 1 mM EDTA, 2  $\mu$ l of 2.0 mg/ml PreScission protease, and 4  $\mu$ l of heparin sodium salt (Nacalai Tesque) per mL of GST-tauRD solution were added to GST-tauRD and incubated at 37°C for 24 h to induce aggregation, and 1 mM DTT, 1 mM EDTA, and 2  $\mu$ l of 2.0 mg/ml PreScission protease per mL of GST- $\alpha$ -Syn solution were added to GST- $\alpha$ -Syn and incubated at 37°C for 1 wk to induce aggregation. The insoluble fraction was separated via centrifugation at 100,000 × g for 1 h and resuspended in PBS by sonication. These recombinant tauRD and  $\alpha$ -Syn fibrils were used to seed tauRD (P301L)-Venus- or  $\alpha$ -Syn (A53T)-Venus-expressing cells or stored at -20°C until use.

### Establishment of tauRD (P301L) and tauFL (P301L) aggregate-positive cell lines

TauRD (P301L)-Venus aggregate-positive cell lines were obtained by transfection of recombinant tauRD fibrils using Lip-ofectamine 2000 (Thermo Fisher Scientific) into HEK293A cells stably expressing tauRD (P301L)-Venus, as previously described (Sanders et al., 2014). Cells were sparsely diluted, and cell lines stably propagating aggregates were selected based on Venus fluorescence measured on Attune NxT Flow Cytometer (Thermo Fisher Scientific). TauRD (P301L)-Flag-Halo aggregate-positive cell lines were generated by stably expressing tauRD (P301L)-Flag-Halo into tauRD (P301L)-Venus aggregate-positive cells. TauRD (P301L)-mCherry aggregate-negative cell lines were generated by stably expressing tauRD (P301L)-mCherry into HEK293A cells. A TauRD (P301L/all-KR)-HA cell line was generated by stably expressing Dox-inducible tauRD (P301L/all-KR)-HA-P2A-iRFP670 into tauRD (P301L)-Venus aggregate-positive cells.

To obtain tauFL (P301L)-Venus aggregate-positive SH-SY5Y cells, sarkosyl-insoluble aggregates derived from tauRD (P301L)-Venus aggregate-expressing HEK293A cells were transfected into SH-SY5Y cells expressing tauFL (P301L)-Venus using Lipofectamine 3000 (Thermo Fisher Scientific). Briefly, tauRD (P301L)-Venus aggregate-positive cells were lysed by lysis buffer (0.1% Triton X-100, 0.5% sarkosyl in PBS) supplemented with 1 mM phenylmethylsulfonyl fluoride to inhibit proteases. Lysates were clarified by centrifugation at 20,000 x g for 20 min, and the supernatant was further ultracentrifuged at 100,000 × q for 1 h using a TLA55 rotor (Beckman Coulter) in Optima MAX Ultracentrifuge (Beckman Coulter) to obtain the sarkosyl-insoluble cell extracts as a pellet. Sarkosyl-insoluble cell extracts from one 10-cm dish of tauRD (P301L)-Venus aggregate-positive HEK293A cells were resuspended in 150-200 ul of PBS and sonicated with a BIORUPTOR (BM Equipment Co., Ltd.) (power setting on "High," for three cycles [30 s "ON," 30 s "OFF"]). 5 µl of Lipofectamine 3000 reagent was suspended in  $50 \,\mu l$  of DMEM and incubated for  $5 \,min$ . Then,  $20 \,\mu l$  of sonicated sarkosyl-insoluble cell extracts in PBS was added and incubated for an additional 20 min. This mixture was then added to SH-SY5Y cells preseeded on a collagen-coated 12-well plate at 50% confluency. This transfection step was repeated two more times in three consecutive days for a total of three transfections, and each time, the cells were reseeded at 50% confluency in a 12-well plate. Maintenance of tauFL (P301L)-Venus aggregates in these



cells was confirmed by microscopy, and they were used for subsequent analyses.

### Establishment of α-Syn (A53T) and PolyQ97 aggregate-positive cell lines

 $\alpha$ -Syn (A53T)-Venus aggregate–positive cell lines were obtained by transfection of recombinant wild-type  $\alpha$ -Syn fibrils using Lipofectamine 2000 (Thermo Fisher Scientific) into HEK293A cells stably expressing  $\alpha$ -Syn (A53T)-Venus. Cells were sparsely diluted, and cell lines stably propagating aggregates were selected based on Venus fluorescence measured on Attune NxT Flow Cytometer (Thermo Fisher Scientific). PolyQ97-Venus aggregate–negative cell lines were generated by stably expressing PolyQ97-Venus into HEK293A cells.

#### **Antibodies**

The following antibodies were used for the study: pan-ubiquitin P4D1 (mouse monoclonal, sc-8017; Santa Cruz), K48-specific ubiquitin Apu2 (rabbit monoclonal, 05-1307; Sigma Millipore), K63-specific ubiquitin Apu3 (rabbit monoclonal, 05-1308; Sigma Millipore), GAPDH 6C5 (mouse monoclonal, sc-32233; Santa Cruz), p97/VCP H-120 (rabbit polyclonal, sc-20700; Santa Cruz), HRS (rabbit polyclonal, A300-989A-T; Bethyl Laboratories), STAM (mouse monoclonal, sc-133093; Santa Cruz), TSG101 EPR7130(B) (rabbit monoclonal, ab125011; Abcam; used for Fig. S2 H and Fig. S4 D), TSG101 (rabbit polyclonal, 28283-1-AP; Proteintech; used for Fig. 3 E; Fig. 7, C and E; Fig. S1 H; Fig. S2 B; Fig. S3, A, B, and E; and Fig. S4 F), UBAP1 (rabbit polyclonal, 12385-1-AP; Proteintech), VPS28 (rabbit polyclonal, 15478-1-AP; Proteintech), VPS37A (rabbit polyclonal, 11870-1-AP; Proteintech), PTPN23 (rabbit polyclonal, 10472-1-AP; Proteintech), VPS22/EAP30 (mouse monoclonal, sc-390747; Santa Cruz), VPS25 (rabbit polyclonal, 15669-1-AP; Proteintech), VPS36 (rabbit polyclonal, 14262-1-AP; Proteintech), CHMP1A (mouse monoclonal, sc-271617; Santa Cruz), CHMP4B (rabbit polyclonal, 42466; Cell Signaling Technology), CHMP4C (mouse polyclonal, ab168205; Abcam), CHMP5 (mouse monoclonal, sc-374338; Santa Cruz), CHMP6 (mouse monoclonal, sc-398963; Santa Cruz), VPS4A (mouse monoclonal, sc-393428; Santa Cruz), VPS4B (mouse monoclonal, sc-377162; Santa Cruz), EEA1 (mouse monoclonal, 610457; BD Transduction Laboratories), LAMP1 (mouse monoclonal, 15665; Cell Signaling Technology), RFP (rabbit polyclonal, PM005; MBL), Flag M2 (mouse monoclonal, F1804; Sigma Millipore), c-Myc A-14 (rabbit polyclonal, sc-789; Santa Cruz), HA (mouse monoclonal, M180-3; MBL), ATG7 (rabbit polyclonal, PM039; MBL), FIP200 (rabbit polyclonal, 17250-1-AP; Proteintech), and LAMP2 (mouse monoclonal, sc-18822; Santa Cruz). The secondary antibodies used were HRP-conjugated anti-mouse IgG + IgM (rabbit polyclonal, 315-035-048; Jackson ImmunoResearch Laboratories), HRP-conjugated anti-rabbit IgG (goat polyclonal, 111-035-144; Jackson ImmunoResearch Laboratories), and Alexa Fluor 647-conjugated anti-mouse (goat polyclonal, A-21236; Invitrogen). Antibody against Venus was raised by immunizing rabbits with recombinant proteins of His-tagged full-length eGFP. Antibodies used to identify proteasome subunits were described previously (Hamazaki et al., 2015; Kaneko et al., 2009; Hirano et al., 2005).

Microautophagy of tau aggregates

#### **Immunoblotting**

Cells were lysed in lysis buffer (20 mM HEPES, pH 7.5, 0.2% Triton X-100, 0.5% glycerol, 100 mM NaCl, 1 mM EDTA) and scraped prior to clarification by centrifugation at 20,000 × g for 20 min. The supernatant was collected as the soluble fraction, while the cell pellet was washed in PBS once and resuspended in buffer containing 0.5% SDS followed by sonication and used as the insoluble fraction. Samples were run on SDS-PAGE gels, transferred to 0.45- $\mu$ m polyvinyl fluoride membranes, and detected using the indicated antibodies. Immunoblots were visualized using a Fusion SL4 system (Vilber Lourmat). Detection of tauRD (P301L)-Venus phosphorylation was performed using Phos-tag acrylamide (AAL-107; FUJIFILM Wako Pure Chemical Corporation) according to the manufacturer's protocols.

### HaloTag pulse-chase

Cells were incubated with TMR ligand (Promega) for 30 min to label the preexisting population of tauRD (P301L)-Flag-Halo before washout. TMR fluorescence intensity was then measured at 0, 12, and 24 h after washout using Attune NxT Flow Cytometer (Thermo Fisher Scientific).

### Proteasome peptidase activity assay

Cells were lysed with NP-40 lysis buffer (25 mM Tris-HCl, pH 7.5, 0.2% (vol/vol) Nonidet P-40, 1 mM DTT, 2 mM ATP, 5 mM MgCl<sub>2</sub>) and clarified by centrifugation at 20,000 × g for 20 min. Peptidase activity was measured using a fluorescent peptide substrate (succinyl-Leu-Leu-Val-Tyr-7-amido-4-methylcoumarin for chymotrypsin-like activity), as described previously (Hamazaki et al., 2015). Briefly, this compound was incubated with the clarified supernatant for 40–60 min at 37°C in 100 mM Tris-HCl buffer (pH 8.0), and the resulting fluorescence of the reaction products was measured by a multimode plate reader Nivo Alpha F (Revvity).

### Immunofluorescence

Cells were fixed in 4% paraformaldehyde for 20 min at room temperature and permeabilized with 0.2% Triton X-100 in PBS. Cells were then mounted with glass coverslips using ProLong Glass (Thermo Fisher Scientific). For immunostaining, cells were blocked with blocking buffer (1% bovine serum albumin, 1% goat serum, 1% glycerol, 0.2% Triton X-100 in PBS) for 60 min at room temperature after permeabilization. Cells were then incubated with primary antibody diluted in blocking buffer overnight at 4°C with rocking, followed by incubation for 1 h with Alexa Fluor 647-conjugated anti-mouse secondary antibody (goat polyclonal, A-21236; Invitrogen) diluted in blocking buffer. Images were obtained with a TCS SP8 confocal microscope with an HCX PL APO 100×/1.40-0.70 OIL objective (Leica Biosystems) using LAS X software or LSM900 or LSM980 with an Airyscan2 super-resolution microscope (ZEISS) with a C Plan-Apochromat 63x/1.4 Oil DIC M27 objective using Zeiss ZEN software (blue edition).

### Detection and quantification of tauRD (P301L)-Venus aggregates by a high-content image analyzer

Detection of the cell nuclei and cytoplasmic aggregates was performed using CellInsight CX5 High-Content Screening (HCS)



Platform (Thermo Fisher Scientific). First, the HEK293A nuclei stained with DAPI were identified and counted using the 350/461-nm wavelength. Following that, the area of DAPI fluorescence was used to define the nucleus (circle) and a region of set width around the nucleus was used as the cytoplasm (ring), which were validated against the bright-field image to correspond to cells. TauRD (P301L)-Venus aggregate signals were detected at 485/521-nm wavelength. Within the ring, the signal of tauRD (P301L)-Venus aggregates was detected as "spots" by HCS Studio Cell Analysis Software (Thermo Fisher Scientific). Finally, the software identifies, counts, and quantifies the pixel intensity of the spots within the ring.

#### Immunoprecipitation

Cells were lysed in IP lysis buffer (20 mM HEPES, pH 7.5, 0.2% Triton X-100, 0.5% glycerol, 100 mM NaCl, 1 mM EDTA) supplemented with 50 mM N-ethylmaleimide to inhibit deubiquitinases and 1 mM phenylmethylsulfonyl fluoride to inhibit proteases, 72 h after transfection, and scraped. Lysates were clarified by centrifugation at 20,000 × q for 20 min, and the supernatant was collected as the soluble fraction. Flagimmunoprecipitation was conducted by incubating the supernatant with anti-Flag M2 Affinity Gel (A2220; Sigma Millipore) for 1 h at 4°C with rotation. Peptides bound to Flag M2 beads were eluted by competition with 1×Flag peptide (041-34584; FUJIFILM Wako Pure Chemical Corporation) or 3×Flag peptide (F4799; Sigma Millipore). For pull-down of tauRD (P301L)-Venus and tauFL (P301L)-Venus, cells were lysed, and the soluble fraction was obtained as in Flag-immunoprecipitation. The insoluble fraction was resuspended in IP buffer containing 0.5% SDS by sonication. The conditioned medium was clarified by centrifugation at 300 × q for 10 min to remove cells, and the supernatant was further centrifuged at 2,000  $\times$  g for 10 min followed by another centrifugation at  $10,000 \times g$  for 30 min to remove dead cells and cell debris. Immunoprecipitation was conducted by incubating the soluble and insoluble fractions or clarified conditioned medium with GST-tagged anti-GFP nanobody for 1 h at 4°C with rotation. Peptides bound to GST-tagged anti-GFP nanobody were eluted by boiling at 95°C for 5 min. GST-tagged anti-GFP nanobody was purified as previously reported (Katoh et al., 2015). Briefly, pGEX-6P-1 GFP-Nanobody was induced with 0.1 mM IPTG at 30°C for 4 h. Cells were lysed in lysis buffer (0.1% Triton X-100, 2 mM DTT in PBS) followed by sonication (10 min, output = 4, duty = 30). Cell lysates were clarified by centrifugation at 10,000 rpm for 10 min twice, applied onto glutathione Sepharose 4B resin (GE Healthcare), and rotated at 4°C for 2 h. Resin was washed with lysis buffer eight times and resuspended in an equal volume of lysis buffer for later use. For pull-down of tauRD (P301L/all-KR)-HA, cells were lysed, and soluble and insoluble fractions were obtained as in GFP-immunoprecipitation. Both fractions were incubated with HA antibody (M180-3; MBL) for 1 h at 4°C with rotation, and immunoprecipitation was conducted by incubating with Protein G Sepharose 4 Fast Flow (Sigma Millipore) for 1 h at 4°C with rotation. Peptides bound to Protein G Sepharose 4 Fast Flow were eluted by boiling at 95°C for 5 min.

### Preparation of the enzymes

The gene encoding the C-terminal His6-tagged human E1 (residues 1-1058) was previously cloned into the pGEX-6P-1 expression vector (Sato et al., 2015). The gene encoding the N-terminal His<sub>6</sub>-tagged SUMO fusion gp78-E2G2 (fusion of the RING domain of human gp78 [residues 227-298] and human E2G2 [residues 1-165]) was cloned into the pET28a expression vector. The genes encoding the N-terminal His6-tagged SUMO fusion of human E2N (residues 3-150), human MMS2 (residues 6-143), and human OTUB1 (residues 2-271) were previously cloned into the pET26b expression vector (Sato et al., 2012). The gene encoding the N-terminal His<sub>6</sub>-tagged GST fusion human AMSH-LP (residues 264–436) was previously cloned into the pCold I expression vector (Sato et al., 2008). Each expression vector was independently transformed into E. coli strain Rosetta 2 (DE3) cells (Novagen), and the cells were cultured in LB medium containing 100 mg/liter ampicillin for the pCold I and pGEX-6P-1 expression vectors or 50 mg/liter kanamycin for the pET26b and pET28a expression vectors at 37°C. When the optical density of the culture at 600 nm reached  $\sim$ 0.5, IPTG was added to a final concentration of 0.1 mM to induce protein expression, and the cells were further cultured for 18 h at 15°C for the pCold expression vector and at 20°C for other expression vectors. The cells were collected by centrifugation at 7,000  $\times$  q for 10 min. The cells were disrupted by sonication in 50 mM Tris-HCl buffer (pH 8.0) containing 150 mM NaCl and 0.5% Triton X-100. The lysates were centrifuged at 30,000  $\times$  g for 60 min. The supernatants were loaded onto a nickel-nitrilotriacetic acid agarose column (Qiagen). The column was washed with 50 mM Tris-HCl buffer (pH 8.0) containing 150 mM NaCl, and the His6-tagged samples were eluted with 50 mM Tris-HCl buffer (pH 8.0) containing 150 mM NaCl and 350 mM imidazole. The samples were further purified by a Resource Q anion exchange column (Cytiva). The purified E1, AMFR-E2G2, E2N, MMS2, AMSH-LP, and OTUB1 were concentrated using an Amicon Ultra-15 10,000 MWCO filter (Sigma Millipore) and stored at -80°C until use.

### Preparation of the ubiquitin chains

Ubiquitin was overproduced in *E. coli* strain Rosetta 2 (DE3) cells (Novagen) transformed with the pET26b harboring the ubiquitin gene in LB medium containing 50 mg/liter kanamycin at 20°C. The cells were collected by centrifugation at 7,000 × g for 10 min. The cells were disrupted by sonication in 50 mM Tris-HCl buffer (pH 8.0) and were incubated for 15 min at 70°C. The lysate was centrifuged at 30,000 × g for 30 min. The supernatant was passed over a Resource Q anion exchange column (Cytiva) pre-equilibrated with 50 mM Tris-HCl buffer (pH 8.0). The flow-through fractions were further purified by HiLoad 16/600 Superdex 75 size-exclusion column (Cytiva) pre-equilibrated with 10 mM Tris-HCl buffer containing 50 mM NaCl. The purified ubiquitin was concentrated to ~50 g/liter using an Amicon Ultra-15 3,000 MWCO filter (Sigma Millipore) and stored at  $-80^{\circ}$ C until use.

For K48-Ub<sub>4</sub> synthesis, ubiquitin (3 mM), E1 (0.7  $\mu$ M), and AMFR-E2G2 (8  $\mu$ M) were mixed in the reaction buffer (50 mM Tris-HCl [pH 9.0] containing 10 mM ATP, 10 mM MgCl<sub>2</sub>, and 0.6 mM DTT) and incubated at 37°C for 20 h. For K63-Ub4



synthesis, ubiquitin (1.5 mM), E1 (0.25  $\mu$ M), E2N (24  $\mu$ M), and MMS2 (24  $\mu$ M) were mixed in the reaction buffer and incubated at 37°C for 3 h. Each reaction solution was mixed with four volumes of 50 mM ammonium acetate buffer (pH 4.5) and purified by Resource S cation exchange column (Cytiva). Peak fractions containing the K48-Ub4 or K63-Ub<sub>4</sub> were buffer-exchanged into 10 mM Tris-HCl (pH 7.5) containing 50 mM NaCl and concentrated to ~20 g/liter using an Amicon Ultra-15 3,000 MWCO filter (Sigma Millipore) and stored at ~80°C until use.

### **UbiCRest assay**

UbiCRest was performed according to a previous report (Hospenthal et al., 2015). Briefly, immunoprecipitation samples were incubated with either OTUB1 (15  $\mu$ M), AMSH-LP (15  $\mu$ M), or OTUB1 plus AMSH-LP (15  $\mu$ M each) in a 20  $\mu$ l of reaction (50 mM Tris-HCl (pH 7.5), 50 mM NaCl, and 5 mM DTT) for 30 min at 37°C. The reaction was stopped by adding SDS buffer and analyzed by immunoblotting. For recombinant ubiquitin chains, 1 mg of K48- or K63-linked tetra ubiquitin was incubated with either OTUB1 (1, 5, or 15  $\mu$ M) or AMSH-LP (1, 5, or 15  $\mu$ M) for 30 min at 37°C. The reaction was stopped by adding SDS buffer and analyzed by either InstantBlue Coomassie Protein Stain (ab119211; Abcam) or immunoblotting.

#### Image processing and analysis

All immunoblots were processed and analyzed by Fiji/ImageJ software (v2.0.0-rc-69/1.52p) (Schindelin et al., 2012). Pixel intensity correlation of tauRD (P301L)-Venus aggregates was calculated by Coloc2 in Fiji/ImageJ via the Pearson method (Pearson's correlation coefficient).

### Statistical analysis

Statistical analyses were performed using Prism 9.0 (GraphPad) software. All statistical information is described in the figure legend. To compare the mean values of two groups, statistical significance was determined by unpaired, two-tailed Student's t test. One-way ANOVA with Dunnett's or Tukey's post hoc test was used for multiple comparisons involving more than two groups. Comparison in HaloTag pulse-chase experiments was made using two-way ANOVA with Bonferroni's post hoc test (Fig. 2, A and B). Data distribution was assumed to be normal, but this was not formally tested.

### Online supplemental material

Fig. S1 shows the establishment and characterization of tauRD (P301L)-Venus aggregate-positive cells. Fig. S1 also shows the list of ESCRT subunits identified by the CRISPR KO screen and that the ESCRT machinery specifically regulates microautophagy of tauRD (P301L). Fig. S2 confirms the KO or knockdown effects of sgRNAs or siRNAs, as well as the expression of sgRNA-resistant variants of ESCRT components shown in Fig. 1. Fig. S3 shows that the secretion and propagation of tauRD (P301L) are extremely limited. Fig. S4 demonstrates that OTUB1 and AMSH-LP are K48- and K63-specific deubiquitinases, respectively. Fig. S4 also confirms the KO or knockdown effects of sgUBAP1 or siTSG101 and the expression of sgRNA-

resistant variants of UBAP1 or siRNA-resistant variants of TSG101 shown in Fig. 4, and reveals that the SOUBA domain in UBAP1 is not responsible for recognizing ubiquitylated tauRD (P301L). Additionally, Fig. S4 shows that TSG101 specifically targets ubiquitylated tauRD (P301L). Fig. S5 confirms the KO effects of sgPTPN23 or sgUBAP1 and the expression of sgRNA-resistant variants of PTPN23 or UBAP1 shown in Figs. 5 and 6. Fig. S5 also shows that ESCRT-mediated microaggrephagy targets  $\alpha$ -Syn (A53T) but not PolyQ97 aggregates. Table S1 lists the vectors used in this study.

### Data availability

The data are available from the corresponding author upon reasonable request.

### **Acknowledgments**

We thank Dr. T. Miyasaka for providing the pRK172-Tau 2N4R vector, Dr. K. Yamano for providing the pBABEpuro 3xFlag-Rab5A (Q79L) and pcDNA3.1 3xFlag-TEV-Rab7A (Q67L) vectors, and Dr. K. Nakayama for providing the pGEX-6P-1 GFP-Nanobody vector. We thank Dr. Y. Hayashi for discussion regarding CHMP4 and VPS4 and providing siRNA sequence for VPS4A. We thank Dr. D. Morito and the University of Tokyo and Carl Zeiss Collaboration Center for letting us use LSM900 or LSM980 with Airyscan2 super-resolution microscope.

This work was supported by JSPS KAKENHI (grant no. JP22H00402 and JP23H04918) and Takeda Science Foundation to S. Murata, JSPS KAKENHI (grant no. 22H04637 and 23H04254) to S. Hirayama, and MEXT Leading Initiative for Excellent Young Researchers and JSPS/MEXT KAKENHI (grant no. JP21H02418 and JP24H01899) to Y. Sato.

Author contributions: Y. Men: conceptualization, formal analysis, investigation, validation, visualization, and writing—original draft, review, and editing. S. Hirayama: conceptualization, formal analysis, funding acquisition, investigation, project administration, resources, supervision, validation, visualization, and writing—original draft, review, and editing. S. Ao: formal analysis and investigation. Y. Shibata: investigation. M. Lo: visualization and writing—review and editing. Y. Sato: resources and writing—original draft, review, and editing. S. Murata: conceptualization, funding acquisition, project administration, supervision, and writing—original draft, review, and editing.

Disclosures: The authors declare no competing interests exist.

Submitted: 20 June 2024 Revised: 9 December 2024 Accepted: 5 March 2025

### References

Agromayor, M., N. Soler, A. Caballe, T. Kueck, S.M. Freund, M.D. Allen, M. Bycroft, O. Perisic, Y. Ye, B. McDonald, et al. 2012. The UBAP1 subunit of ESCRT-I interacts with ubiquitin via a SOUBA domain. *Structure*. 20: 414–428. https://doi.org/10.1016/j.str.2011.12.013

Arii, J., M. Watanabe, F. Maeda, N. Tokai-Nishizumi, T. Chihara, M. Miura, Y. Maruzuru, N. Koyanagi, A. Kato, and Y. Kawaguchi. 2018. ESCRT-III

n et al. Journal of Cell Biology 20 of 23



- mediates budding across the inner nuclear membrane and regulates its integrity. *Nat. Commun.* 9:3379. https://doi.org/10.1038/s41467-018-05889-9
- Baietti, M.F., Z. Zhang, E. Mortier, A. Melchior, G. Degeest, A. Geeraerts, Y. Ivarsson, F. Depoortere, C. Coomans, E. Vermeiren, et al. 2012. Syndecan-syntenin-ALIX regulates the biogenesis of exosomes. Nat. Cell Biol. 14:677–685. https://doi.org/10.1038/ncb2502
- Barghorn, S., Q. Zheng-Fischhöfer, M. Ackmann, J. Biernat, M. von Bergen, E.M. Mandelkow, and E. Mandelkow. 2000. Structure, microtubule interactions, and paired helical filament aggregation by tau mutants of frontotemporal dementias. *Biochemistry*. 39:11714–11721. https://doi.org/ 10.1021/bi000850r
- Bejarano, E., and A.M. Cuervo. 2010. Chaperone-mediated autophagy. Proc. Am. Thorac. Soc. 7:29–39. https://doi.org/10.1513/pats.200909-102JS
- Benyair, R., S.S.P. Giridharan, P. Rivero-Ríos, J. Hasegawa, E. Bristow, E.-L. Eskelinen, M.D. Shmueli, V. Fishbain-Yoskovitz, Y. Merbl, L.M. Sharkey, et al. 2023. Upregulation of the ESCRT pathway and multivesicular bodies accelerates degradation of proteins associated with neuro-degeneration. Autophagy Rep. 2:2166722. https://doi.org/10.1080/27694127.2023.2166722
- von Bergen, M., S. Barghorn, L. Li, A. Marx, J. Biernat, E.M. Mandelkow, and E. Mandelkow. 2001. Mutations of tau protein in frontotemporal dementia promote aggregation of paired helical filaments by enhancing local  $\beta$ -structure. *J. Biol. Chem.* 276:48165–48174. https://doi.org/10.1074/jbc.M105196200
- Bourinaris, T., D. Smedley, V. Cipriani, I. Sheikh, A. Athanasiou-Fragkouli, P. Chinnery, H. Morris, R. Real, V. Harrison, E. Reid, et al. 2020. Identification of UBAP1 mutations in juvenile hereditary spastic paraplegia in the 100,000 Genomes Project. *Eur. J. Hum. Genet.* 28:1763–1768. https://doi.org/10.1038/s41431-020-00720-w
- Caballero, B., M. Bourdenx, E. Luengo, A. Diaz, P.D. Sohn, X. Chen, C. Wang, Y.R. Juste, S. Wegmann, B. Patel, et al. 2021. Acetylated tau inhibits chaperone-mediated autophagy and promotes tau pathology propagation in mice. *Nat. Commun.* 12:2238. https://doi.org/10.1038/s41467-021-22501-9
- Ceresa, B.P., M. Lotscher, and S.L. Schmid. 2001. Receptor and membrane recycling can occur with unaltered efficiency despite dramatic Rab5(q79l)-induced changes in endosome geometry. *J. Biol. Chem.* 276: 9649–9654. https://doi.org/10.1074/jbc.M010387200
- Chen, J.J., D.L. Nathaniel, P. Raghavan, M. Nelson, R. Tian, E. Tse, J.Y. Hong, S.K. See, S.A. Mok, M.Y. Hein, et al. 2019. Compromised function of the ESCRT pathway promotes endolysosomal escape of tau seeds and propagation of tau aggregation. J. Biol. Chem. 294:18952–18966. https:// doi.org/10.1074/jbc.RA119.009432
- Ciechanover, A., and Y.T. Kwon. 2015. Degradation of misfolded proteins in neurodegenerative diseases: Therapeutic targets and strategies. Exp. Mol. Med. 47:e147. https://doi.org/10.1038/emm.2014.117
- Cone, A.S., S.N. Hurwitz, G.S. Lee, X. Yuan, Y. Zhou, Y. Li, and D.G. Meckes Jr. 2020. Alix and Syntenin-1 direct amyloid precursor protein trafficking into extracellular vesicles. *BMC Mol. Cell Biol.* 21:58. https://doi.org/10.1186/s12860-020-00302-0
- Cripps, D., S.N. Thomas, Y. Jeng, F. Yang, P. Davies, and A.J. Yang. 2006. Alzheimer disease-specific conformation of hyperphosphorylated paired helical filament-Tau is polyubiquitinated through Lys-48, Lys-11, and Lys-6 ubiquitin conjugation. *J. Biol. Chem.* 281:10825-10838. https://doi.org/10.1074/jbc.M512786200
- Darwich, N.F., J.M. Phan, B. Kim, E. Suh, J.D. Papatriantafyllou, L. Changolkar, A.T. Nguyen, C.M. O'Rourke, Z. He, S. Porta, et al. 2020. Autosomal dominant VCP hypomorph mutation impairs disaggregation of PHFtau. Science. 370:eaay8826. https://doi.org/10.1126/science.aay8826
- Doyotte, A., A. Mironov, E. McKenzie, and P. Woodman. 2008. The Bro1-related protein HD-PTP/PTPN23 is required for endosomal cargo sorting and multivesicular body morphogenesis. *Proc. Natl. Acad. Sci. USA*. 105:6308–6313. https://doi.org/10.1073/pnas.0707601105
- Eliezer, D., P. Barré, M. Kobaslija, D. Chan, X. Li, and L. Heend. 2005. Residual structure in the repeat domain of tau: Echoes of microtubule binding and paired helical filament formation. *Biochemistry*. 44:1026–1036. https://doi.org/10.1021/bi048953n
- Fändrich, M., S. Nyström, K.P.R. Nilsson, A. Böckmann, H. LeVine, and P. Hammarström. 2018. Amyloid fibril polymorphism: A challenge for molecular imaging and therapy. J. Intern. Med. 283:218–237. https://doi.org/10.1111/joim.12732
- Farazi Fard, M.A., A.P. Rebelo, E. Buglo, H. Nemati, H. Dastsooz, I. Gehweiler, S. Reich, J. Reichbauer, B. Quintáns, A. Ordóñez-Ugalde, et al. 2019. Truncating mutations in UBAP1 cause hereditary spastic paraplegia.

- Am. J. Hum. Genet. 104:767-773. https://doi.org/10.1016/j.ajhg.2019.05 .009
- Ferrer, I., I. López-González, M. Carmona, L. Arregui, E. Dalfó, B. Torrejón-Escribano, R. Diehl, and G.G. Kovacs. 2013. Glial and neuronal tau pathology in tauopathies: Characterization of disease-specific phenotypes and tau pathology progression. J. Neuropathol. Exp. Neurol. 73:81–97. https://doi.org/10.1097/NEN.000000000000000
- Gahloth, D., G. Heaven, T.A. Jowitt, A.P. Mould, J. Bella, C. Baldock, P. Woodman, and L. Tabernero. 2017. The open architecture of HD-PTP phosphatase provides new insights into the mechanism of regulation of ESCRT function. Sci. Rep. 7:9151. https://doi.org/10.1038/s41598-017-09467-9
- Gahloth, D., C. Levy, G. Heaven, F. Stefani, L. Wunderley, P. Mould, M.J. Cliff, J. Bella, A.J. Fielding, P. Woodman, and L. Tabernero. 2016. Structural basis for selective interaction between the ESCRT regulator HD-PTP and UBAP1. Structure. 24:2115–2126. https://doi.org/10.1016/j.str.2016.10 .006
- Ghossoub, R., F. Lembo, A. Rubio, C.B. Gaillard, J. Bouchet, N. Vitale, J. Slavík, M. Machala, and P. Zimmermann. 2014. Syntenin-ALIX exosome biogenesis and budding into multivesicular bodies are controlled by ARF6 and PLD2. Nat. Commun. 5:3477. https://doi.org/10.1038/ncomms4477
- Goodwin, J.M., W.E. Dowdle, R. DeJesus, Z. Wang, P. Bergman, M. Kobylarz, A. Lindeman, R.J. Xavier, G. McAllister, B. Nyfeler, et al. 2017. Autophagy-independent lysosomal targeting regulated by ULK1/2-FIP200 and ATG9. Cell Rep. 20:2341–2356. https://doi.org/10.1016/j.celrep.2017.08.034
- Grundke-Iqbal, I., K. Iqbal, Y.-C. Tung, M. Quinlan, H.M. Wisniewski, and L.I. Bindert. 1986. Abnormal phosphorylation of the microtubule-associated protein X (tau) in Alzheimer cytoskeletal pathology. Proc. Natl. Acad. Sci. USA. 83. 4913-4917. https://doi.org/10.1073/pnas.83.13.4913
- Gu, S., C.A. Chen, J.A. Rosenfeld, H. Cope, N. Launay, K.M. Flanigan, M.A. Waldrop, R. Schrader, J. Juusola, O. Goker-Alpan, et al. 2020. Truncating variants in UBAP1 associated with childhood-onset non-syndromic hereditary spastic paraplegia. *Hum. Mutat.* 41:632–640. https://doi.org/10.1002/humu.23950
- Hamazaki, J., S. Hirayama, and S. Murata. 2015. Redundant roles of Rpn10 and Rpn13 in recognition of ubiquitinated proteins and cellular homeostasis. PLoS Genet. 11:e1005401. https://doi.org/10.1371/journal.pgen.1005401
- Hart, T., A.H.Y. Tong, K. Chan, J. Van Leeuwen, A. Seetharaman, M. Aregger, M. Chandrashekhar, N. Hustedt, S. Seth, A. Noonan, et al. 2017. Evaluation and design of genome-wide CRISPR/SpCas9 knockout screens. G3: Genes, Genomes. G3. 7:2719–2727. https://doi.org/10.1534/g3.117.041277
- Hirano, Y., K.B. Hendil, H. Yashiroda, S. Iemura, R. Nagane, Y. Hioki, T. Natsume, K. Tanaka, and S. Murata. 2005. A heterodimeric complex that promotes the assembly of mammalian 20S proteasomes. *Nature*. 437:1381–1385. https://doi.org/10.1038/nature04106
- Hospenthal, M.K., T.E.T. Mevissen, and D. Komander. 2015. Deubiquitinase-based analysis of ubiquitin chain architecture using Ubiquitin Chain Restriction (UbiCRest). Nat. Protoc. 10:349–361. https://doi.org/10.1038/nprot.2015.018
- Ichioka, F., E. Takaya, H. Suzuki, S. Kajigaya, V.L. Buchman, H. Shibata, and M. Maki. 2007. HD-PTP and Alix share some membrane-traffic related proteins that interact with their Brol domains or proline-rich regions. Arch. Biochem. Biophys. 457:142-149. https://doi.org/10.1016/j.abb.2006 .11.008
- Joung, J., S. Konermann, J.S. Gootenberg, O.O. Abudayyeh, R.J. Platt, M.D. Brigham, N.E. Sanjana, and F. Zhang. 2017. Genome-scale CRISPR-Cas9 knockout and transcriptional activation screening. Nat. Protoc. 12: 828–863. https://doi.org/10.1038/nprot.2017.016
- Kametani, F., M. Tahira, M. Takao, T. Matsubara, K. Hasegawa, M. Yoshida, Y. Saito, S. Murayama, and M. Hasegawa. 2024. Analysis and comparison of post-translational modifications of α-synuclein filaments in multiple system atrophy and dementia with Lewy bodies. Sci. Rep. 14: 22892. https://doi.org/10.1038/s41598-024-74130-z
- Kaneko, T., J. Hamazaki, S. Iemura, K. Sasaki, K. Furuyama, T. Natsume, K. Tanaka, and S. Murata. 2009. Assembly pathway of the Mammalian proteasome base subcomplex is mediated by multiple specific chaperones. Cell. 137:914–925. https://doi.org/10.1016/j.cell.2009.05.008
- Katoh, Y., S. Nozaki, D. Hartanto, R. Miyano, and K. Nakayama. 2015. Architectures of multisubunit complexes revealed by a visible immuno-precipitation assay using fluorescent fusion proteins. J. Cell Sci. 128: 2351–2362. https://doi.org/10.1242/jcs.168740
- Katsinelos, T., M. Zeitler, E. Dimou, A. Karakatsani, H.M. Müller, E. Nachman, J.P. Steringer, C. Ruiz de Almodovar, W. Nickel, and T.R. Jahn. 2018.



- Unconventional secretion mediates the trans-cellular spreading of tau. *Cell Rep.* 23:2039–2055. https://doi.org/10.1016/j.celrep.2018.04.056
- Kaushik, S., and A.M. Cuervo. 2018. The coming of age of chaperone-mediated autophagy. Nat. Rev. Mol. Cell Biol. 19:365-381. https://doi.org/10.1038/s41580-018-0001-6
- Kitamura, A., H. Kubota, C.G. Pack, G. Matsumoto, S. Hirayama, Y. Takahashi, H. Kimura, M. Kinjo, R.I. Morimoto, and K. Nagata. 2006. Cytosolic chaperonin prevents polyglutamine toxicity with altering the aggregation state. Nat. Cell Biol. 8:1163–1170. https://doi.org/10.1038/ncb1478
- Kuchitsu, Y., and T. Taguchi. 2023. Lysosomal microautophagy: An emerging dimension in mammalian autophagy. Trends Cell Biol. https://doi.org/10 .1016/j.tcb.2023.11.005
- Kyalu Ngoie Zola, N., C. Balty, S. Pyr Dit Ruys, A.A.T. Vanparys, N.D.G. Huyghe, G. Herinckx, M. Johanns, E. Boyer, P. Kienlen-Campard, M.H. Rider, et al. 2023. Specific post-translational modifications of soluble tau protein distinguishes Alzheimer's disease and primary tauopathies. Nat. Commun. 14:3706. https://doi.org/10.1038/s41467-023-39328-1
- Lee, M.J., J.H. Lee, and D.C. Rubinsztein. 2013. Tau degradation: The ubiquitin-proteasome system versus the autophagy-lysosome system. *Prog. Neurobiol.* 105:49–59. https://doi.org/10.1016/j.pneurobio.2013.03.001
- Li, W., J. Köster, H. Xu, C.H. Chen, T. Xiao, J.S. Liu, M. Brown, and X.S. Liu. 2015. Quality control, modeling, and visualization of CRISPR screens with MAGeCK-VISPR. Genome Biol. 16:281. https://doi.org/10.1186/ s13059-015-0843-6
- Lin, X., H.Z. Su, E.L. Dong, X.H. Lin, M. Zhao, C. Yang, C. Wang, J. Wang, Y.J. Chen, H. Yu, et al. 2019. Stop-gain mutations in UBAP1 cause pure autosomal-dominant spastic paraplegia. *Brain*. 142:2238–2252. https://doi.org/10.1093/brain/awz158
- Majumder, P., and O. Chakrabarti. 2016. ESCRTs and associated proteins in lysosomal fusion with endosomes and autophagosomes. *Biochem. Cell Biol.* 94:443–450. https://doi.org/10.1139/bcb-2016-0099
- Martinez-Vicente, M., Z. Talloczy, S. Kaushik, A.C. Massey, J. Mazzulli, E.V. Mosharov, R. Hodara, R. Fredenburg, D.C. Wu, A. Follenzi, et al. 2008. Dopamine-modified α-synuclein blocks chaperone-mediated autophagy. J. Clin. Invest. 118:777–788. https://doi.org/10.1172/JCI32806
- Mee Hayes, E., L. Sirvio, and Y. Ye. 2022. A potential mechanism for targeting aggregates with proteasomes and disaggregases in liquid droplets. Front. Aging Neurosci. 14:854380. https://doi.org/10.3389/fnagi.2022.854380
- Merezhko, M., C.A. Brunello, X. Yan, H. Vihinen, E. Jokitalo, R.L. Uronen, and H.J. Huttunen. 2018. Secretion of tau via an unconventional nonvesicular mechanism. *Cell Rep.* 25:2027–2035.e4. https://doi.org/10.1016/j.celrep.2018.10.078
- Mukherjee, A., B. Patel, H. Koga, A.M. Cuervo, and A. Jenny. 2016. Selective endosomal microautophagy is starvation-inducible in Drosophila. Autophagy. 12:1984–1999. https://doi.org/10.1080/15548627.2016.1208887
- Nagai, T., K. Ibata, E.S. Park, M. Kubota, K. Mikoshiba, and A. Miyawaki. 2002. A variant of yellow fluorescent protein with fast and efficient maturation for cell-biological applications. *Nat. Biotechnol.* 20:87–90. https://doi.org/10.1038/nbt0102-87
- Nakajima, H., F. Kimura, T. Nakagawa, D. Furutama, and N. Ohsawa. 1996.

  Transcriptional activation by the androgen receptor in X-linked spinal and bulbar muscular atrophy. *J. Neurol Sci.* 142. 12–16. https://doi.org/10
- Nan, H., Y. Ichinose, M. Tanaka, K. Koh, H. Ishiura, J. Mitsui, H. Mizukami, M. Morimoto, S. Hamada, T. Ohtsuka, et al. 2019. UBAP1 mutations cause juvenile-onset hereditary spastic paraplegias (SPG80) and impair UBAP1 targeting to endosomes. J. Hum. Genet. 64:1055–1065. https://doi.org/10.1038/s10038-019-0670-9
- Natale, F., S. Fusco, and C. Grassi. 2022. Dual role of brain-derived extracellular vesicles in dementia-related neurodegenerative disorders: Cargo of disease spreading signals and diagnostic-therapeutic molecules. *Transl. Neurodegener.* 11:50. https://doi.org/10.1186/s40035-022-00326-w
- Oku, M., and Y. Sakai. 2018. Three distinct types of microautophagy based on membrane dynamics and molecular machineries. *BioEssays*. 40: e1800008. https://doi.org/10.1002/bies.201800008
- Parkinson, M.D.J., S.C. Piper, N.A. Bright, J.L. Evans, J.M. Boname, K. Bowers, P.J. Lehner, and J.P. Luzio. 2015. A non-canonical ESCRT pathway, including histidine domain phosphotyrosine phosphatase (HD-PTP), is used for down-regulation of virally ubiquitinated MHC class I. Biochem. J. 471:79–88. https://doi.org/10.1042/BJ20150336
- Polanco, J.C., and J. Götz. 2022. Exosomal and vesicle-free tau seeds-propagation and convergence in endolysosomal permeabilization. FEBS J. 289:6891-6907. https://doi.org/10.1111/febs.16055

- Rollinson, S., P. Rizzu, S. Sikkink, M. Baker, N. Halliwell, J. Snowden, B.J. Traynor, D. Ruano, N. Cairns, J.D. Rohrer, et al. 2009. Ubiquitin associated protein 1 is a risk factor for frontotemporal lobar degeneration. Neurobiol. Aging. 30:656-665. https://doi.org/10.1016/j.neurobiolaging.2009.01.009
- Rossi, G., and F. Tagliavini. 2015. Frontotemporal lobar degeneration: Old knowledge and new insight into the pathogenetic mechanisms of tau mutations. Front. Aging Neurosci. 7:192. https://doi.org/10.3389/fnagi .2015.00192
- Sahu, R., S. Kaushik, C.C. Clement, E.S. Cannizzo, B. Scharf, A. Follenzi, I. Potolicchio, E. Nieves, A.M. Cuervo, and L. Santambrogio. 2011. Microautophagy of cytosolic proteins by late endosomes. *Dev. Cell.* 20: 131–139. https://doi.org/10.1016/j.devcel.2011.02.011
- Saito, T., T. Chiku, M. Oka, S. Wada-Kakuda, M. Nobuhara, T. Oba, K. Shinno, S. Abe, A. Asada, A. Sumioka, et al. 2021. Disulfide bond formation in microtubule-associated tau protein promotes tau accumulation and toxicity in vivo. Hum. Mol. Genet. 30:1955-1967. https://doi.org/10.1093/hmg/ddab162
- Sakai, Y., and M. Oku. 2024. ATG and ESCRT control multiple modes of microautophagy. FEBS Lett. 598:48-58. https://doi.org/10.1002/1873 -3468.14760
- Sanders, D.W., S.K. Kaufman, S.L. DeVos, A.M. Sharma, H. Mirbaha, A. Li, S.J. Barker, A.C. Foley, J.R. Thorpe, L.C. Serpell, et al. 2014. Distinct tau prion strains propagate in cells and mice and define different tauopathies. *Neuron.* 82:1271–1288. https://doi.org/10.1016/j.neuron.2014.04.047
- Sato, Y., E. Goto, Y. Shibata, Y. Kubota, A. Yamagata, S. Goto-Ito, K. Kubota, J. Inoue, M. Takekawa, F. Tokunaga, and S. Fukai. 2015. Structures of CYLD USP with Met1- or Lys63-linked diubiquitin reveal mechanisms for dual specificity. Nat. Struct. Mol. Biol. 22:222–229. https://doi.org/10.1038/nsmb.2970
- Sato, Y., A. Yamagata, S. Goto-Ito, K. Kubota, R. Miyamoto, S. Nakada, and S. Fukai. 2012. Molecular basis of Lys-63-linked polyubiquitination inhibition by the interaction between human deubiquitinating enzyme OTUB1 and ubiquitin-conjugating enzyme UBC13. J. Biol. Chem. 287: 25860–25868. https://doi.org/10.1074/jbc.M112.364752
- Sato, Y., A. Yoshikawa, A. Yamagata, H. Mimura, M. Yamashita, K. Ookata, O. Nureki, K. Iwai, M. Komada, and S. Fukai. 2008. Structural basis for specific cleavage of Lys 63-linked polyubiquitin chains. *Nature*. 455: 358–362. https://doi.org/10.1038/nature07515
- Schindelin, J., I. Arganda-Carreras, E. Frise, V. Kaynig, M. Longair, T. Pietzsch, S. Preibisch, C. Rueden, S. Saalfeld, B. Schmid, et al. 2012. Fiji: An open-source platform for biological-image analysis. *Nat. Methods.* 9: 676–682. https://doi.org/10.1038/nmeth.2019
- Shimura, H., D. Schwartz, S.P. Gygi, and K.S. Kosik. 2004. CHIP-Hsc70 complex ubiquitinates phosphorylated tau and enhances cell survival. J. Biol. Chem. 279:4869-4876. https://doi.org/10.1074/jbc.M305838200
- Skowyra, M.L., P.H. Schlesinger, T.V. Naismith, and P.I. Hanson. 2018. Triggered recruitment of ESCRT machinery promotes endolysosomal repair. Science. 360:eaar5078. https://doi.org/10.1126/science.aar5078
- Stefani, F., L. Zhang, S. Taylor, J. Donovan, S. Rollinson, A. Doyotte, K. Brownhill, J. Bennion, S. Pickering-Brown, and P. Woodman. 2011. UBAP1 is a component of an endosome-specific ESCRT-I complex that is essential for MVB sorting. Curr. Biol. 21:1245–1250. https://doi.org/10.1016/j.cub.2011.06.028
- Strang, K.H., C.L. Croft, Z.A. Sorrentino, P. Chakrabarty, T.E. Golde, and B.I. Giasson. 2018. Distinct differences in prion-like seeding and aggregation between Tau protein variants provide mechanistic insights into tauopathies. J. Biol. Chem. 293:2408–2421. https://doi.org/10.1074/jbc.AAC118.002657
- Strickland, M., S. Watanabe, S.M. Bonn, C.M. Camara, M.R. Starich, D. Fushman, C.A. Carter, and N. Tjandra. 2022. Tsg101/ESCRT-I recruitment regulated by the dual binding modes of K63-linked diubiquitin. Structure. 30:289–299.e6. https://doi.org/10.1016/j.str.2021.09.006
- Sundquist, W.I., H.L. Schubert, B.N. Kelly, G.C. Hill, J.M. Holton, and C.P. Hill. 2004. Ubiquitin recognition by the human TSG101 protein. Mol. Cell. 13: 783–789. https://doi.org/10.1016/S1097-2765(04)00129-7
- Sweeney, P., H. Park, M. Baumann, J. Dunlop, J. Frydman, R. Kopito, A. McCampbell, G. Leblanc, A. Venkateswaran, A. Nurmi, and R. Hodgson. 2017. Protein misfolding in neurodegenerative diseases: Implications and strategies. *Transl. Neurodegener*. 6:6. https://doi.org/10.1186/s40035-017-0077-5
- Szymańska, E., P. Nowak, K. Kolmus, M. Cybulska, K. Goryca, E. Derezińska-Wołek, A. Szumera-Ciećkiewicz, M. Brewińska-Olchowik, A. Grochowska, K. Piwocka, et al. 2020. Synthetic lethality between VPS4A

https://doi.org/10.1083/jcb.202406120

Nen et al. Journal of Cell Biology 22 of 23



- and VPS4B triggers an inflammatory response in colorectal cancer. EMBO Mol. Med. 12:e10812. https://doi.org/10.15252/emmm.201910812
- Tang, S., N.J. Buchkovich, M. Henne, S. Banjade, Y.J. Kim, and S.D. Emr. 2016. ESCRT-III activation by parallel action of ESCRT-I/II and ESCRT-0/Brol during MVB biogenesis. Elife. 5:e15507. https://doi.org/10.7554/eLife .15507
- Tekirdag, K., and A.M. Cuervo. 2018. Chaperone-mediated autophagy and endosomal microautophagy: Joint by a chaperone. *J. Biol. Chem.* 293: 5414–5424. https://doi.org/10.1074/jbc.R117.818237
- Uemura, N., M.T. Uemura, K.G. Luk, V.M.Y. Lee, and J.Q. Trojanowski. 2020. Cell-to-Cell transmission of tau and α-synuclein. *Trends Mol. Med.* 26: 936–952. https://doi.org/10.1016/j.molmed.2020.03.012
- Vaz-Silva, J., P. Gomes, Q. Jin, M. Zhu, V. Zhuravleva, S. Quintremil, T. Meira, J. Silva, C. Dioli, C. Soares-Cunha, et al. 2018. Endolysosomal degradation of Tau and its role in glucocorticoid-driven hippocampal malfunction. EMBO J. 37:e99084. https://doi.org/10.15252/embj.201899084
- Vietri, M., M. Radulovic, and H. Stenmark. 2020. The many functions of ESCRTs. Nat. Rev. Mol. Cell Biol. 21:25–42. https://doi.org/10.1038/ s41580-019-0177-4
- Waltho, A., O. Popp, C. Lenz, L. Pluska, M. Lambert, V. Dötsch, P. Mertins, and T. Sommer. 2024. K48- and K63-linked ubiquitin chain interactome

- reveals branch- and length-specific ubiquitin interactors. *Life Sci. Alliance*. 7:e202402740. https://doi.org/10.26508/lsa.202402740
- Wang, J., Y. Hou, L. Qi, S. Zhai, L. Zheng, L. Han, Y. Guo, B. Zhang, P. Miao, Y. Lou, et al. 2020. Autosomal dominant hereditary spastic paraplegia caused by mutation of UBAP1. Neurogenetics. 21:169–177. https://doi.org/10.1007/s10048-020-00608-3
- Wharton, S.B., C.J. McDermott, A.J. Grierson, J.D. Wood, C. Gelsthorpe, P.G. Ince, and P.J. Shaw. 2003. The cellular and molecular pathology of the motor system in hereditary spastic paraparesis due to mutation of the spastin gene. J. Neuropathol. Exp. Neurol. 62:1166–1177. https://doi.org/10.1093/jnen/62.11.1166
- Wilkinson, M., Y. Xu, D. Thacker, A.I.P. Taylor, D.G. Fisher, R.U. Gallardo, S.E. Radford, and N.A. Ranson. 2023. Structural evolution of fibril polymorphs during amyloid assembly. Cell. 186:5798–5811.e26. https://doi.org/10.1016/j.cell.2023.11.025
- Williams, R.L., and S. Urbé. 2007. The emerging shape of the ESCRT machinery. Nat. Rev. Mol. Cell Biol. 8:355-368. https://doi.org/10.1038/nrm2162
- Wunderley, L., K. Brownhill, F. Stefani, L. Tabernero, and P. Woodman. 2014. The molecular basis for selective assembly of the UBAP1-containing endosome-specific ESCRT-I complex. J. Cell Sci. 127:663–672. https://doi.org/10.1242/jcs.140673



### Supplemental material

S2



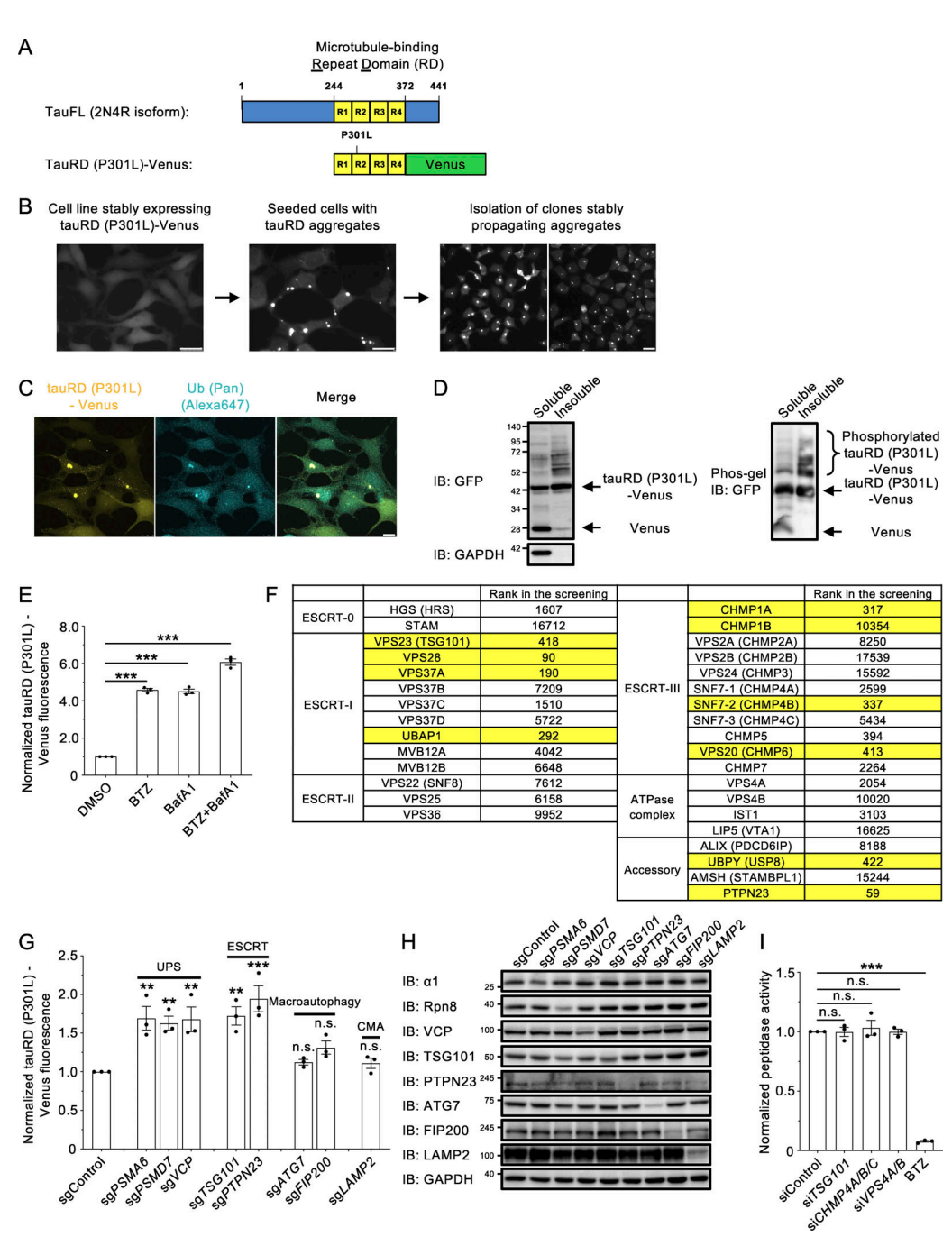


Figure S1. Supplementary material to Fig. 1. (A) Schematic view of 2N4R isoform of full-length tau and tauRD (P301L)-Venus constructs. (B) Schematic diagram for the establishment of cell lines stably propagating tauRD (P301L)-Venus aggregates. Scale bar: 25 μm. (C) Immunofluorescence-based staining of ubiquitin chain in tauRD (P301L)-Venus aggregate-positive cells. Images were acquired by a confocal microscope. Scale bar: 10 µm. (D) TauRD (P301L)-Venus aggregate-positive cells were lysed, and soluble and insoluble fractions were immunoblotted with the indicated antibodies. For detection of tauRD (P301L)-Venus phosphorylation, samples were run in gels supplemented with Phos-tag acrylamide (Phos-gel). (E) TauRD (P301L)-Venus aggregate-positive cells were treated with 500 nM BTZ, 1 µM BafA1, or both BTZ and BafA1 for 24 h, and tauRD (P301L)-Venus fluorescence was measured by flow cytometry. Data were normalized to the Venus fluorescence of DMSO-treated cells and represent the mean  $\pm$  SEM (n = 3, from three independent experiments). Significance was calculated using one-way ANOVA with Dunnett's test with \*\*\*P < 0.001. (F) List of ESCRT machinery subunits that were identified in the CRISPR KO screen. The β-score ranks are noted in the column to the right of the protein name. Positive hits are highlighted in yellow. (G and H) TauRD (P301L)-Venus aggregate-positive cells were transfected with control or individual sgRNA, as indicated, and successfully transfected cells were selected by puromycin treatment. TauRD (P301L)-Venus fluorescence was measured by flow cytometry (G), and whole-cell lysates were immunoblotted with the indicated antibodies 1 wk after transfection (H). Data were normalized to the Venus fluorescence sgControl-treated cells and represent the mean ± SEM (n = 3, from three independent experiments). Significance was calculated using one-way ANOVA with Dunnett's test with \*\*P < 0.01, \*\*\*P < 0.001. n.s. not significant. (I) HEK293A cells were transfected with control or individual siRNA, as indicated, or treated with 500 nM BTZ for 3 h. Cells were lysed 72 h after transfection or 3 h after drug treatment, and the proteasome chymotrypsin-like activity was measured. Data were normalized to the proteasome chymotrypsin-like activity of siControl-treated cells and represent the mean ± SEM (n = 3, from three independent experiments). Significance was calculated using one-way ANOVA with Dunnett's test with \*\*\*P < 0.001. n.s., not significant. Source data are available for this figure: SourceData FS1.



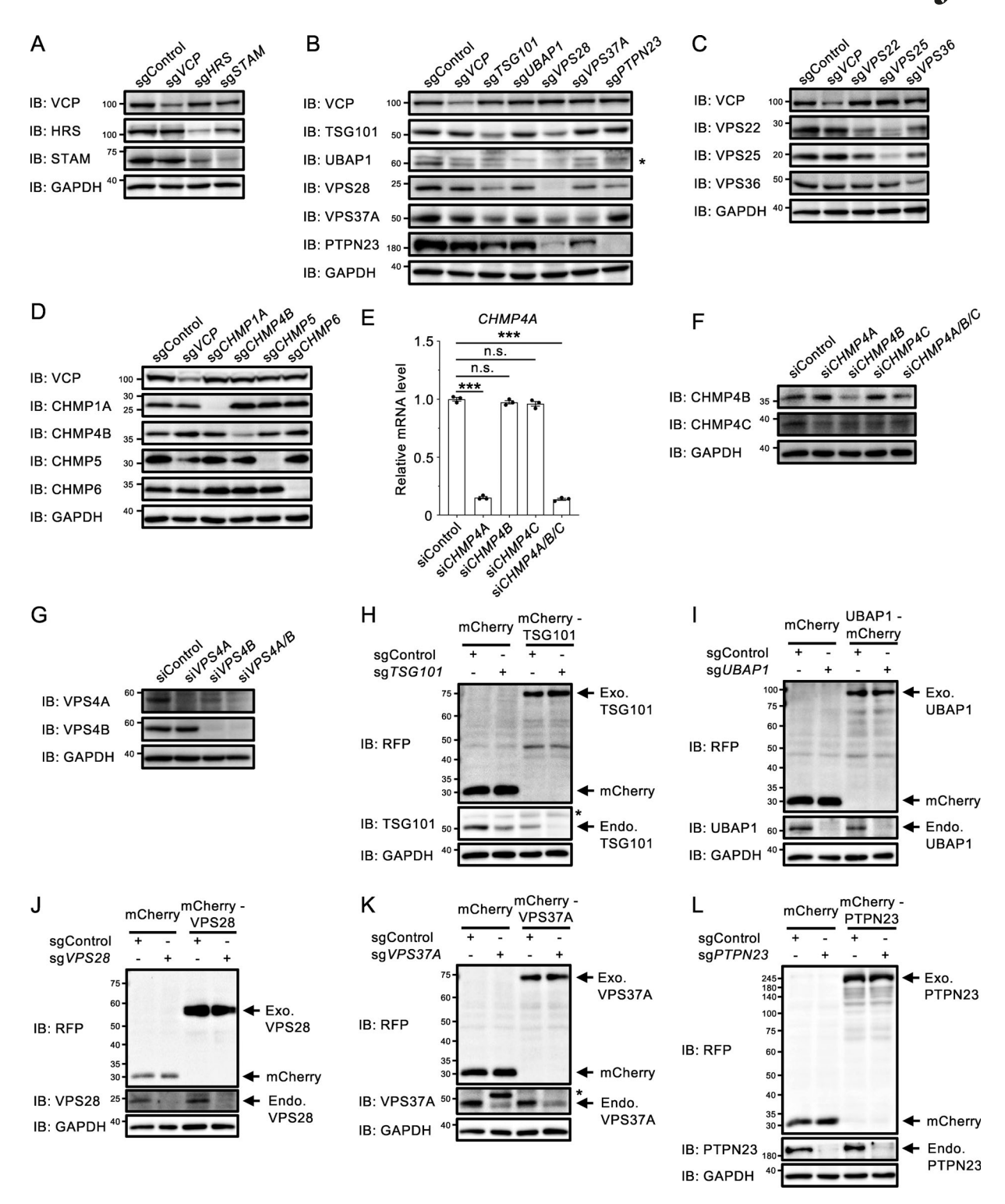


Figure S2. KO or knockdown confirmation to Fig. 1. (A-D) TauRD (P301L)-Venus aggregate-positive cells were transfected with control or individual sgRNA, as indicated, and successfully transfected cells were selected by puromycin treatment. Whole-cell lysates were immunoblotted with the indicated antibodies 1 wk after transfection. (E) TauRD (P301L)-Venus aggregate-positive cells were transfected with control or individual siRNA, as indicated. Expression levels of the CHMP4A gene were measured by quantitative PCR 72 h after transfection. Data were normalized to the expression level of CHMP4A in siControl-treated cells and represent the mean ± SEM (n = 3, from three independent experiments). Significance was calculated using one-way ANOVA with Dunnett's test with \*\*\*P < 0.001. n.s., not significant. (F and G) TauRD (P301L)-Venus aggregate-positive cells were transfected with control or individual siRNA, as indicated. Whole-cell lysates were immunoblotted with the indicated antibodies 72 h after transfection. (H-L) TauRD (P301L)-Venus aggregatepositive cells stably expressing mCherry (Control) or mCherry-tagged sgRNA-resistant variants of TSG101, UBAP1, VPS28, VPS37A, and PTPN23 were transfected with individual sgRNA of ESCRT-I complex subunits, and successfully transfected cells were selected by puromycin treatment. Whole-cell lysates were immunoblotted with the indicated antibodies 1 wk after transfection. The asterisk denotes a nonspecific band. Source data are available for this figure: SourceData FS2.

Men et al. Journal of Cell Biology Microautophagy of tau aggregates

S3

**S4** 



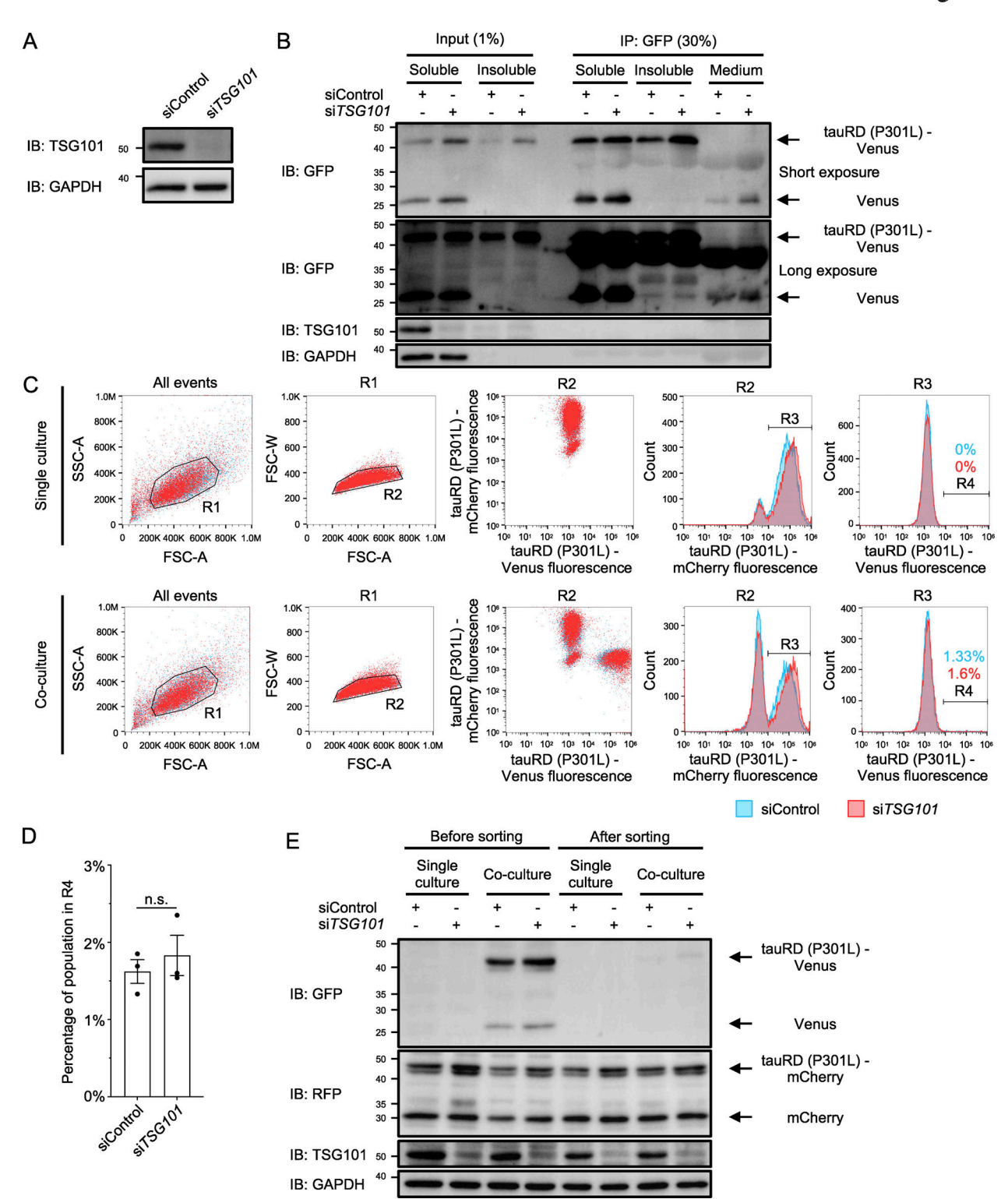


Figure S3. Supplementary material to Fig. 2. (A) HEK293A cells were transfected with control or TSG101 siRNA, and whole-cell lysates were immunoblotted with the indicated antibodies 72 h after transfection. (B) TauRD (P301L)-Venus aggregate-positive cells were transfected with control or TSG101 siRNA. Cells were lysed 72 h after transfection, and Triton X-100-soluble and Triton X-100-insoluble fractions and the conditioned medium were immunoprecipitated using a GST-tagged anti-GFP nanobody. Input and IP samples at the indicated percentages were immunoblotted with the indicated antibodies. (C) Single-cultured tauRD (P301L)-mCherry aggregate-negative cells, or cocultured tauRD (P301L)-mCherry aggregate-negative cells and tauRD (P301L)-Venus aggregatepositive cells were transfected with control or TSG101 siRNA. Cells were analyzed by flow cytometry 72 h after transfection. TauRD (P301L)-Venus fluorescence in tauRD (P301L)-mCherry cells was gated as R4. (D) Quantification of tauRD (P301L)-Venus fluorescence in R4. Data were normalized to the Venus fluorescence in siControl-treated cells and represent the mean  $\pm$  SEM (n=3, from three independent experiments). Significance was calculated using two-tailed Student's t test with n.s., not significant. (E) Single-cultured or cocultured cells in C were sorted for tauRD (P301L)-mCherry-positive population by flow cytometry and immunoblotted with the indicated antibodies. Source data are available for this figure: SourceData FS3.

Men et al. Journal of Cell Biology Microautophagy of tau aggregates



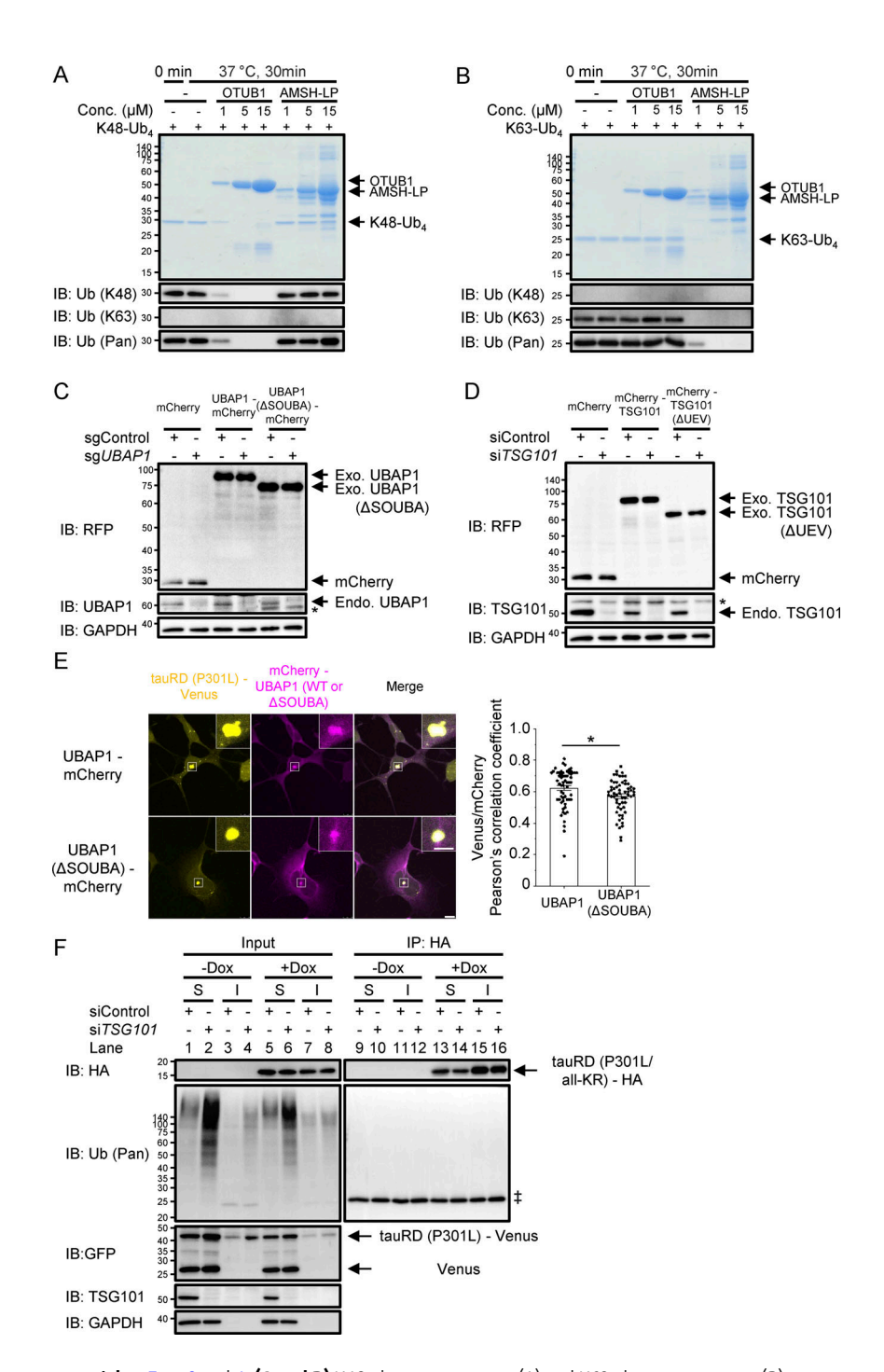


Figure S4. Supplementary material to Figs. 3 and 4. (A and B) K48 ubiquitin tetramer (A) and K63 ubiquitin tetramer (B) were treated with OTUB1 or AMSH-LP at the indicated concentrations and rotated at 37°C for 30 min and then analyzed on an SDS-PAGE gel or immunoblotted with the indicated antibodies. (C) TauRD (P301L)-Venus aggregate-positive cells stably expressing mCherry (control) or mCherry-tagged sgRNA-resistant variants of WT UBAP1 and UBAP1 (ASOUBA) were transfected with control or UBAP1 sgRNA, and successfully transfected cells were selected by puromycin selection. Whole-cell lysates were immunoblotted with the indicated antibodies 1 wk after transfection. (D) TauRD (P301L)-Venus aggregate-positive cells stably expressing mCherry (control) or mCherry-tagged siRNA-resistant variants of WT TSG101 and TSG101 (ΔUEV) were transfected with control or TSG101 siRNA. Whole-cell lysates were immunoblotted with the indicated antibodies 72 h after transfection. (E) Visualization of tauRD (P301L)-Venus aggregates and UBAP1 and UBAP1 (ΔSOUBA) in cells stably expressing mCherry-tagged WT UBAP1 and UBAP1 (\Delta SOUBA). Endogenous UBAP1 was depleted by sgRNA KO. Images were acquired by a confocal microscope, and boxed areas are magnified at the top right corner. Pixel intensity correlation of tauRD (P301L)-Venus aggregates was calculated. Data represent the mean  $\pm$  SEM (n = 60, from three independent experiments, 20 cells per experiment). Significance was calculated using two-tailed Student's t test with \*P < 0.05. Scale bar: 10 and 5 μm (magnified images). (F) TauRD (P301L)-Venus aggregate-positive cells stably expressing Tet-on tauRD (P301L/all-KR)-HA-P2A-iRFP670 aggregate-positive cells were transfected with control or TSG101 siRNA. 1 μl/ml Dox was added at the time of transfection. Cells were lysed 72 h after transfection, and Triton X-100-soluble and Triton X-100-insoluble fractions were immunoprecipitated with a HA antibody. Input and IP samples were immunoblotted with the indicated antibodies with S, soluble, and I, insoluble. The asterisk denotes a nonspecific band. A double dagger denotes the light chain of Protein G. Source data are available for this figure: SourceData FS4.

Men et al. Journal of Cell Biology Microautophagy of tau aggregates

S5



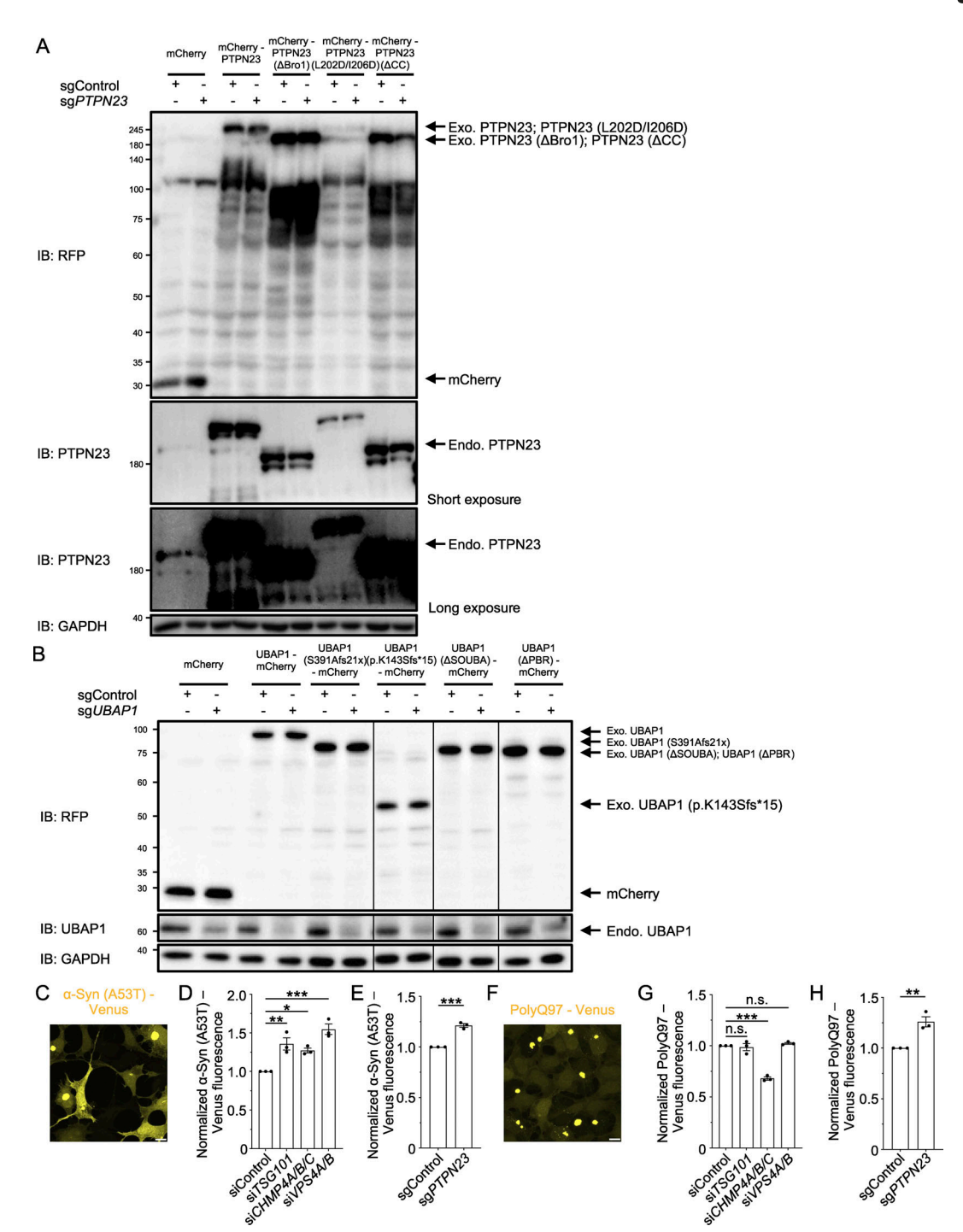


Figure S5. **Supplementary material to** Figs. 5, 6, and 7. **(A and B)** TauRD (P301L)-Venus aggregate–positive cells stably expressing mCherry, mCherry-tagged sgRNA-resistant PTPN23 proteins illustrated in Fig. 5 A (A), or mCherry-tagged sgRNA-resistant UBAP1 proteins illustrated in Fig. 6 A (B) were transfected with control or *UBAP1* sgRNA (A), or control or *PTPN23* sgRNA (B), and successfully transfected cells were selected by puromycin selection. Whole-cell lysates were immunoblotted with the indicated antibodies 1 wk after transfection. **(C)** Representative image of  $\alpha$ -Syn (A53T)-Venus aggregate–positive cells. Scale bar: 10  $\mu$ m. **(D and E)**  $\alpha$ -Syn (A53T)-Venus aggregate–positive cells were transfected with control, *TSG101*, *CHMP4A/B/C*, or *VPS4A/B* siRNA (D), or transfected with control or *PTPN23* sgRNA, and successfully transfected cells were selected by puromycin treatment (E).  $\alpha$ -Syn (A53T)-Venus fluorescence was measured by flow cytometry 72 h (D) or 1 wk (E) after transfection. Data were normalized to the Venus fluorescence of siControl (D)- or sgControl (E)-treated cells and represent the mean  $\pm$  SEM (n = 3, from three independent experiments). Significance was calculated using one-way ANOVA with Dunnett's test (D) or two-tailed Student's t test (E) with \*P < 0.05, \*\*P < 0.01, \*\*\*P < 0.001. **(F)** Representative image of PolyQ97-Venus aggregate–positive cells. Scale bar: 10  $\mu$ m. **(G and H)** PolyQ97-Venus aggregate–positive cells were transfected with control, *TSG101*, *CHMP4A/B/C*, or *VPS4A/B* siRNA (G), or transfected with control or *PTPN23* sgRNA, and successfully transfected cells were selected by puromycin treatment (H). PolyQ97-Venus fluorescence was measured by flow cytometry 72 h (G) or 1 wk (H) after transfection. Data were normalized to the Venus fluorescence of siControl (G)- or sgControl (H)-treated cells and represent the mean  $\pm$  SEM (n = 3, from three independent experiments). Significance was calculated using one-way ANOVA with Dunnett's test (G) or two-tailed Studen

Men et al. Journal of Cell Biology

S6



Provided online is Table S1. Table S1 lists the vectors used in this study.